CLUH controls astrin-1 expression to couple mitochondrial metabolism to cell cycle progression — **Source link** [↗]

Désirée Schatton, Giada Di Pietro, Karolina Szczepanowska, Matteo Veronese ...+9 more authors

Institutions: University of Cologne, Max Planck Society

Related papers:

- Phosphorylation of cell cycle proteins at senescence

- Mitotic phosphorylation of the ULK complex regulates cell cycle progression.

- Human mitochondrial Fis1 links to cell cycle regulators at G2/M transition

- Transcriptional down-regulation of metabolic genes by Gdown1 ablation induces quiescent cell re-entry into the cell cycle.

- Glucose restriction induces transient G2 cell cycle arrest extending cellular chronological lifespan

Share this paper: [f] [y] [in] [✉]

View more about this paper here: https://typeset.io/papers/cluh-controls-astrin-1-expression-to-couple-mitochondrial-zsd5gehzec

1 **CLUH controls astrin-1 expression to couple mitochondrial**

2 **metabolism to cell cycle progression**

3

4 **Désirée Schatton[1,2], Giada Di Pietro[1,2], Karolina Szczepanowska[2,3,#], Matteo Veronese[1,2],**

5 **Marie-Charlotte Marx[1,2], Kristina Braunöhler[1,2], Esther Barth[1,2], Stefan Müller[2], Patrick**

6 **Giavalisco[4], Thomas Langer[2,4], Aleksandra Trifunovic[2,3,5] and Elena I. Rugarli[1,2,5*]**

7

8 [1]Institute for Genetics, University of Cologne, Cologne 50931, Germany

9 [2]Cologne Excellence Cluster on Cellular Stress Responses in Aging-Associated Diseases

10 (CECAD), Cologne 50931, Germany

11 [3] Institute for Mitochondrial Diseases and Ageing, University of Cologne, Cologne 50931,

12 Germany

13 [4] Max Planck Institute for Biology of Ageing, Cologne 50931, Germany.

14 [5]Center for Molecular Medicine (CMMC), University of Cologne, Cologne 50931, Germany.

15 [#] Present address: ReMedy International Research Agenda Unit, IMol Polish Academy of

16 Sciences, Warsaw, Poland

17

18 *Correspondence: elena.rugarli@uni-koeln.de

19

20

Abstract

Proliferating cells undergo metabolic changes in synchrony with cell cycle progression and cell division. Mitochondria provide fuel, metabolites, and ATP during different phases of the cell cycle, however it is not completely understood how mitochondrial function and the cell cycle are coordinated. CLUH is a post-transcriptional regulator of mRNAs encoding mitochondrial proteins involved in oxidative phosphorylation and several metabolic pathways. Here, we show a role of CLUH in regulating the expression of astrin, which is involved in metaphase to anaphase progression, centrosome integrity, and mTORC1 inhibition. We find that CLUH binds both the *SPAG5* mRNA and its product astrin, and controls the synthesis and the stability of the full-length astrin-1 isoform. We show that CLUH interacts with astrin-1 specifically during interphase. Astrin-depleted cells show mislocalized CLUH at focal adhesions, mTORC1 hyperactivation and enhanced anabolism. On the other hand, cells lacking CLUH show decreased astrin levels and increased mTORC1 signaling, but cannot sustain anaplerotic and anabolic pathways. In absence of CLUH, cells fail to grow during G1, and progress faster through the cell cycle, indicating dysregulated matching of growth, metabolism and cell cycling. Our data reveal a role of CLUH in coupling growth signaling pathways and mitochondrial metabolism with cell cycle progression.

Introduction

40 Proliferating cells adjust their metabolism to each individual phase of the cell cycle

41 (DeBerardinis et al, 2008; Buchakjian & Kornbluth, 2010; Lee & Finkel, 2013; Salazar-Roa &

42 Malumbres, 2017). Before division cells must double their biomass and DNA content. This

43 entails a prominent rewiring of metabolism to foster biosynthetic pathways allowing the

44 synthesis of nucleic acids, proteins and lipids. During mitosis, an increase in ATP production

45 supplies the energy needed for pulling apart and segregating the chromosomes. As metabolic

46 organelles, mitochondria are key actors in the metabolic reprogramming of proliferating cells.

47 On the one hand, cell cycle regulators influence mitochondrial metabolism in various ways

48 (Leal-Esteban & Fajas, 2020). For example, CDK1 phosphorylates components of the

49 respiratory chain during G2 and of the mitochondrial translocase of the outer membrane during

50 mitosis, probably to enhance oxidative respiration and ATP production (Harbauer et al, 2014;

51 Wang et al, 2014). On the other hand, energy deficiency is sensed by cell cycle checkpoints

52 causing cell cycle arrest (Mandal et al, 2005; Salazar-Roa & Malumbres, 2017). Mitochondrial

53 dynamics is also intimately linked to cell cycle progression. A hyperfused mitochondrial

54 network is important for the G1-S transition, while mitochondria must fragment before cells

55 enter mitosis (Mitra et al, 2009). Therefore, proliferating cells depend on several coordinated

56 mechanisms to regulate how mitochondria utilize nutrients to fuel cell growth or energy

57 production during the cell cycle. However, how mitochondrial metabolism and respiratory

58 function are coordinated during the cell cycle is still largely unclear. Unravelling these

59 mechanisms is crucial since they are often dysregulated in cancer.

60 One of the ways how mitochondrial metabolism can be rewired is through regulation of RNA

61 regulons by RNA-binding proteins (Schatton & Rugarli, 2018). CLUH (clustered mitochondria

62 homologue) is a conserved RNA-binding protein, which binds transcripts encoding proteins

63 involved in the respiratory chain, the TCA cycle, and other mitochondrial metabolic pathways

64   (Gao et al, 2014). Upon loss of CLUH, target mRNAs are subjected to faster decay and their

65   respective proteins are decreased in abundance (Schatton et al, 2017). This leads to alterations

66   in mitochondrial distribution (mitochondrial clustering as the gene name alludes to)

67   mitochondrial cristae integrity, respiratory defects, loss of mtDNA, and decreased activity of

68   TCA cycle enzymes (Schatton et al, 2017; Wakim et al, 2017; Pla-Martin et al, 2020). In the

69   mouse, constitutive loss of *Cluh* causes neonatal lethality, while a liver-specific *Cluh* knock-

70   out (KO) led to hypoglycemia and defective ketogenesis upon starvation (Schatton et al, 2017).

71   CLUH and its target mRNAs form ribonucleoprotein particles in primary hepatocytes. These

72   CLUH granules are important not only to protect target mRNAs from degradation, but also to

73   restrict mTORC1 activation and promote mitophagy (Pla-Martin et al, 2020). Thus, in post-

74   mitotic hepatocytes CLUH controls the balance between catabolism and anabolism, allowing a

75   survival response to starvation.

76   Astrin (also called SPAG5) is a multifunctional protein with a well-established role during

77   mitosis. The complex astrin/kinastrin/DYNLL1 is involved in the stabilization of the

78   kinetochore-microtubule interactions in metaphase (Kern et al, 2017). Consistently, cells

79   lacking astrin or its interactor kinastrin show defects in chromosome segregations and a delayed

80   metaphase to anaphase progression (Gruber et al, 2002; Dunsch et al, 2011). Astrin has however

81   other roles in interphase, ranging from mTORC1 inhibition (Thedieck et al, 2013), centrosome

82   integrity and centriole duplication (Thein et al, 2007; Kodani et al, 2015), and regulation of p53

83   levels during G2 after DNA damage (Halim et al, 2013). Astrin is highly expressed in several

84   cancers and it is considered a poor prognostic marker (Yuan et al, 2014; Abdel-Fatah et al,

85   2016; Bertucci et al, 2016; Zhou et al, 2018; Ying et al, 2020).

86   We show here that in HeLa cells astrin exists in two isoforms, astrin-1 and astrin-2. We reveal

87   that CLUH binds the *SPAG5* mRNA, as well as the astrin-1 protein. The interaction of CLUH

88   and astrin-1 occurs during interphase and protects astrin-1 and kinastrin from degradation.

4

89   Moreover, we show that CLUH positively regulates mitochondrial anaplerotic pathways that

90   sustain mTORC1 activation. Our data disclose a role of CLUH in coupling mitochondrial

91   metabolism to cell cycle progression.

Results

CLUH interacts with astrin-1 and kinastrin

94   We previously showed that CLUH binds several mRNAs for mitochondrial proteins (Gao et al,

95   2014). However, among CLUH-bound transcripts, we found *SPAG5* encoding astrin, a

96   multifunctional protein involved in metaphase to anaphase progression, centrosome integrity

97   and mTORC1 regulation (Gruber et al, 2002; Thein et al, 2007; Schmidt et al, 2010; Dunsch et

98   al, 2011; Thedieck et al, 2013; Gao et al, 2014; Kodani et al, 2015). Surprisingly, we also

99   detected astrin as an RNA-independent interactor of endogenous CLUH in a pull-down

100   experiment in HeLa cells after stable isotope labeling in cell culture (SILAC) followed by mass

101   spectrometry (Supplementary Table 1). Reciprocal immunoprecipitations (IPs) using

102   antibodies against human CLUH and astrin, followed by western blot, confirmed the interaction

103   (Figure 1A). Binding was also validated between CLUH and kinastrin (also known as SKAP),

104   a known astrin interactor (Figure 1B) (Schmidt et al, 2010; Dunsch et al, 2011).

105   Astrin appears as two isoforms (hereafter referred to as astrin-1 and astrin-2) in western blots,

106   and CLUH interacts preferentially with the slower migrating isoform, astrin-1 (Figure 1A). The

107   existence of these two isoforms has been reported in the literature but their identity remains

108   enigmatic. On closer inspection of the *SPAG5* mRNA, we noticed the presence of five in-frame

109   ATGs downstream of the first ATG (hereafter referred to as ATG2-6), which could serve as

110   alternative translation start codons (with moderate and good Kozak sequences) (Figure 1C).

111   Moreover, an upstream ORF within the *SPAG5* 5' UTR (Figure 1C) could influence translation

112   from the downstream ATGs as reported for other genes (Morris & Geballe, 2000; Young &

113   Wek, 2016). To test these hypotheses, we produced different constructs expressing the 5' UTR

114   and the coding region of the *SPAG5* cDNA, and we mutagenized the uATG, the ATG1 or

115   downstream ATGs individually or in different combinations to GGG (Figure 1-figure

116   supplement 1A). When we expressed the uATG^{GGG}-SPAG5 construct, the expression of astrin-

117   2 was suppressed (Figure 1D). Furthermore, mutagenesis of ATG1 confirmed the existence of

118   a downstream alternative translation start site (Figure 1D). Overexpression of the constructs

119   harboring mutagenized downstream ATGs revealed that astrin-2 is the product of alternative

120   translation starting from ATG3-5 (Figure 1E). The identity of astrin-1 was also confirmed by

121   pull-down of this isoform only using an antibody directed against the N-terminal region of the

122   protein (Figure 1-figure supplement 1B).

123   To evaluate whether the interaction domain of astrin that binds to CLUH lies in the N-terminal

124   part of astrin-1, we transfected a construct expressing both astrin-1 and astrin-2 (ATG1-SPAG5,

125   Figure 1-figure supplement 1A) or an N-terminus deleted variant (Δ151-SPAG5, Figure 1-

126   figure supplement 1A) and performed reciprocal IPs in HeLa wildtype and *CLUH* KO cells

127   (Wakim et al, 2017) (Figure 1F). An interaction was observed only with full-length astrin,

128   proving that CLUH binds within the N-terminus of astrin-1 (Figure 1F). In contrast, the astrin

129   interactor kinastrin has no binding preference to any of the two astrin isoforms, consistent with

130   the previously mapped interaction domain between these two proteins (residues 482-693 of

131   astrin) (Figure 1-figure supplement 1C) (Dunsch et al, 2011; Friese et al, 2016; Kern et al, 2016;

132   Kern et al, 2017). CLUH still interacts with astrin-1 upon kinastrin depletion, suggesting that

133   kinastrin is not required for the interaction (Figure 1-figure supplement 1D). In polysome

134   profiles performed after chemical crosslinking, CLUH migrated in lighter fractions, as well as

135   in fractions containing the monosome and polysomes (Figure 1G). In contrast, astrin and

136   kinastrin were only detected in the lighter fractions (Figure 1G).

6

137
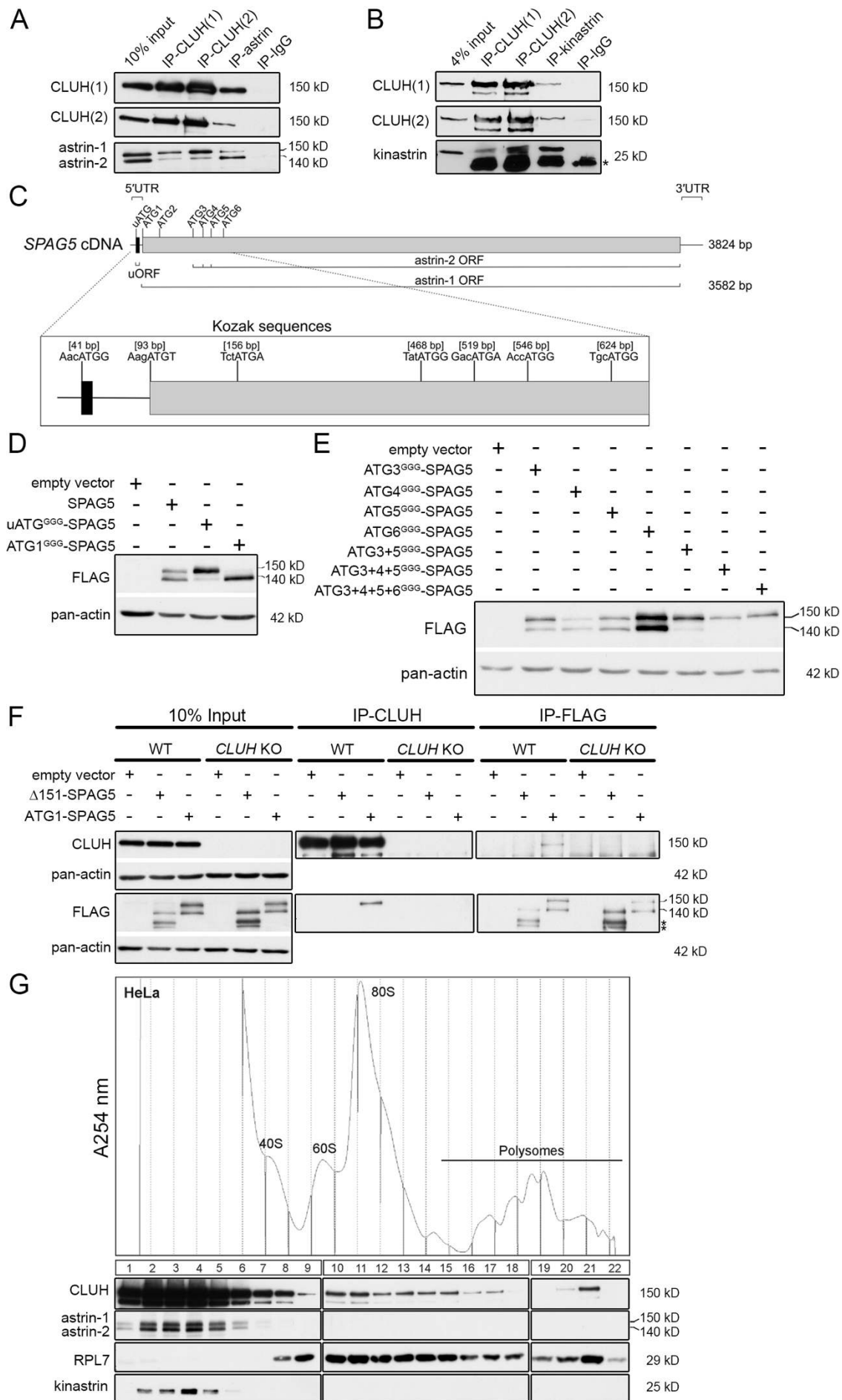
Figure 1. CLUH interacts with astrin-1 and kinastrin.

(**A, B**) Western blots of reciprocal co-IPs of endogenous CLUH, astrin and kinastrin in HeLa cells. Two different antibodies have been used to pull down CLUH (1, 2). Asterisks mark IgG light chain. (**C**) Scheme of human *SPAG5* cDNA with indicated UTRs and ORFs. Close up shows positions of the uATG and ATG1-6 with surrounding Kozak sequences. (**D, E**) Western blots of HeLa cells overexpressing FLAG-tagged astrin constructs. Pan-actin was used as loading control. (**F**) Western blots of reciprocal co-IPs of endogenous CLUH and overexpressed FLAG-tagged astrin full length (ATG1-SPAG5) or a N-terminal deleted variant (Δ151-SPAG5) in WT and *CLUH* KO HeLa cells. Pan-actin was used as loading control for input samples. Asterisks indicate additional astrin bands appearing upon overexpression of the N-terminal deleted variant. (**G**) Polysome profiling of HeLa cells chemically crosslinked with DSP. At the top, absorbance profile at 254 nm of the fractions is shown with indicated peaks of 40S and 60S ribosomal subunits, 80S monosome and polysomes; at the bottom the corresponding western blots of the fractions are shown. RPL7 was used as a marker for ribosomes.

In conclusion, we identify the expression of two astrin isoforms via alternative initiation of translation, and establish CLUH as a specific molecular partner of astrin-1.

CLUH controls astrin-1 and kinastrin stability and astrin expression

In absence of CLUH, kinastrin and astrin-1, but not astrin-2, are decreased in abundance (Figure 2A). To investigate whether CLUH influences the stability of its interaction partners, we performed a cycloheximide (CHX) chase in wildtype and *CLUH* KO HeLa cells (Figure 2A). In absence of CLUH, kinastrin and astrin-1, but not astrin-2, are highly unstable (Figure 2A-D). The instability of astrin in absence of CLUH was confirmed in *Cluh* KO MEFs which only express the larger isoform of astrin (Figure 2-figure supplement 1A, B). Inhibition of the proteasome by MG132 treatment in *CLUH* KO HeLa cells fully rescued kinastrin and partially astrin-1 levels (Figure 2A, E-G). Decreased kinastrin levels upon astrin depletion have already been reported (Schmidt et al, 2010; Dunsch et al, 2011).

The underlying reason for the only partial rescue of astrin-1 might be another level of regulation by CLUH. Given the identification of *SPAG5* mRNA as a CLUH target (Gao et al, 2014), we tested if CLUH is involved in astrin synthesis. To this end, we immunoprecipitated newly

167   synthesized astrin in wildtype and *CLUH* KO cells after labeling with ^{35}S methionine for

168   different time points (Figure 2H-I). We observed that CLUH regulates the synthesis of astrin-

169   1 (Figure 2H-I). CLUH controls the expression of some of its target mRNAs by preventing their

170   degradation (Schatton et al., 2017). To elucidate whether this is also the case for *SPAG5*, we

171   labeled newly synthesized RNA with the uridine analog ethynyl uridine (EU) and chased it for

172   8 h. We precipitated the EU-RNA with biotin-azide using Click-iT chemistry and quantified

173   *SPAG5* mRNA levels with qRT-PCR. *SPAG5* mRNA was less stable in absence of CLUH,

174   whereas steady state levels and EU incorporation were unaffected (Figure 2J-L).
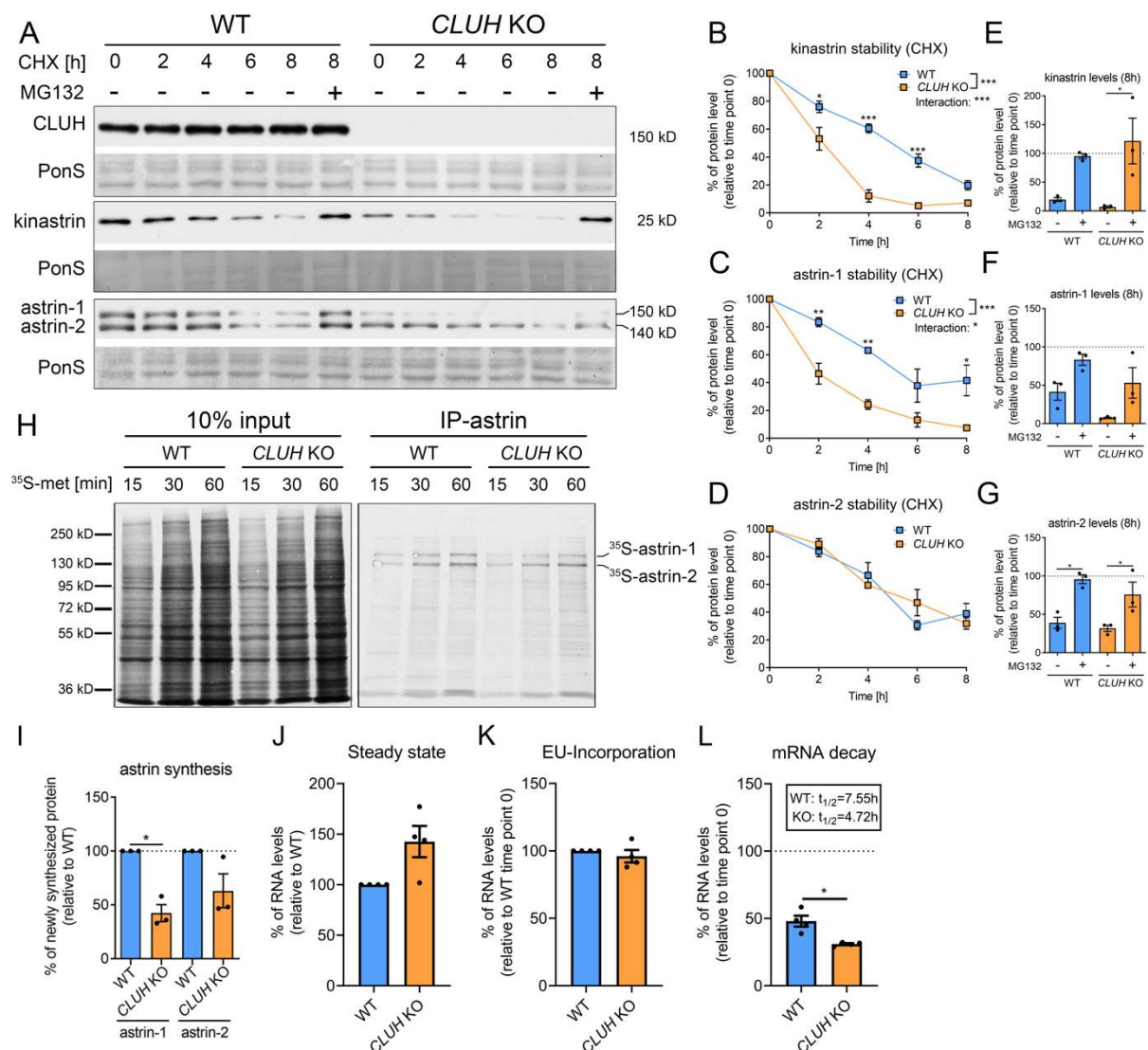
176   **Figure 2. CLUH controls astrin-1 and kinastrin stability and astrin expression.**

9

177   (**A**) Western blots of WT and *CLUH* KO HeLa cells treated with CHX for indicated time points with or

178   w/o additional MG132 treatment. Ponceau S staining was used as loading control. (**B-D**) Quantification

179   of CHX chase western blots as shown in A (n=3 independent experiments). Two-way ANOVA with

180   post hoc Tukey`s multiple comparison tests were performed with P≤0.05: *; P≤0.01: **; P≤0.001: ***.

181   Genotype x time interaction significance is also shown. Error bars represent SEM. (**E-G**) Quantification

182   of proteins levels after 8 h CHX treatment of western blots as shown in A (n=3 independent

183   experiments). Bars show the mean ± SEM. Dotted lines indicate protein levels at 0h time points. One-

184   way ANOVA with post hoc Tukey`s multiple comparison tests were performed with P≤0.05: *. (**H**)

185   Autoradiograms of IP of newly synthesized astrin labeled with ^{35}S-methionine for indicated time points

186   in WT and *CLUH* KO HeLa cells. (**I**) Quantification of immunoprecipitated newly synthesized astrin

187   after 60 min labeling of experiments as shown in H (n=3 independent experiments). Bars show the mean

188   ± SEM. Two-tailed paired Student's t-test was performed with P≤0.05: *. (**J**) Steady state mRNA levels

189   of *SPAG5* in WT and *CLUH* KO HeLa cells (n=4 independent experiments). Bars show mean ± SEM.

190   *RPL13* levels have been used for normalization. (**K, L**) Levels of EU-incorporation (K) and mRNA

191   decay (L) of *SPAG5* mRNA in WT and *CLUH* KO HeLa cells after specific labeling and pull down of

192   newly synthesized RNA (n=4 independent experiments). *GAPDH* levels have been used for

193   normalization. Calculated half-lives are indicated. Bars show the mean ± SEM. Two-tailed paired

194   Student's t-test was performed with P≤0.05: *.

195   In conclusion, our data reveal that CLUH controls the expression of astrin-1 at multiple levels,

196   by binding and stabilizing its mRNA, by affecting its synthesis, and maintaining its stability.

CLUH binds astrin-1 in interphase

198   Astrin controls cell cycle progression at various stages, raising the question if the complex

199   CLUH-astrin-1 is cell cycle-dependent. To this end, we immunoprecipitated CLUH from cells

200   enriched in different phases of the cell cycle (Figure 3A, Figure 3-supplement 1A). The

201   effective synchronization of the cells was confirmed by analyzing the input levels of cyclin D3

202   (G2 phase marker), pH3-Ser10 (M phase marker) and pRPS6-Ser235/236 (inhibited upon

203   starvation) (Figure 3A). Astrin-1, but not astrin-2, was more abundant in S and G2, while CLUH

204   levels were similar in the different phases of the cell cycle (Figure 3A). Both astrin isoforms

205   are phosphorylated at multiple sites, leading to slower migration in SDS-PAGE in

206   prometaphase (PM) (Figure 3A) (Chang et al, 2001; Cheng et al, 2008; Chiu et al, 2014; Chung

207   et al, 2016; Geraghty et al, 2021). The CLUH/astrin-1 complex is enriched in S and G2 phases

208   but not detected in PM, indicating that CLUH preferentially interacts with unmodified astrin-1

209   in interphase and that the interaction might be controlled by the phosphorylation status of astrin

210   (Figure 3A).

211
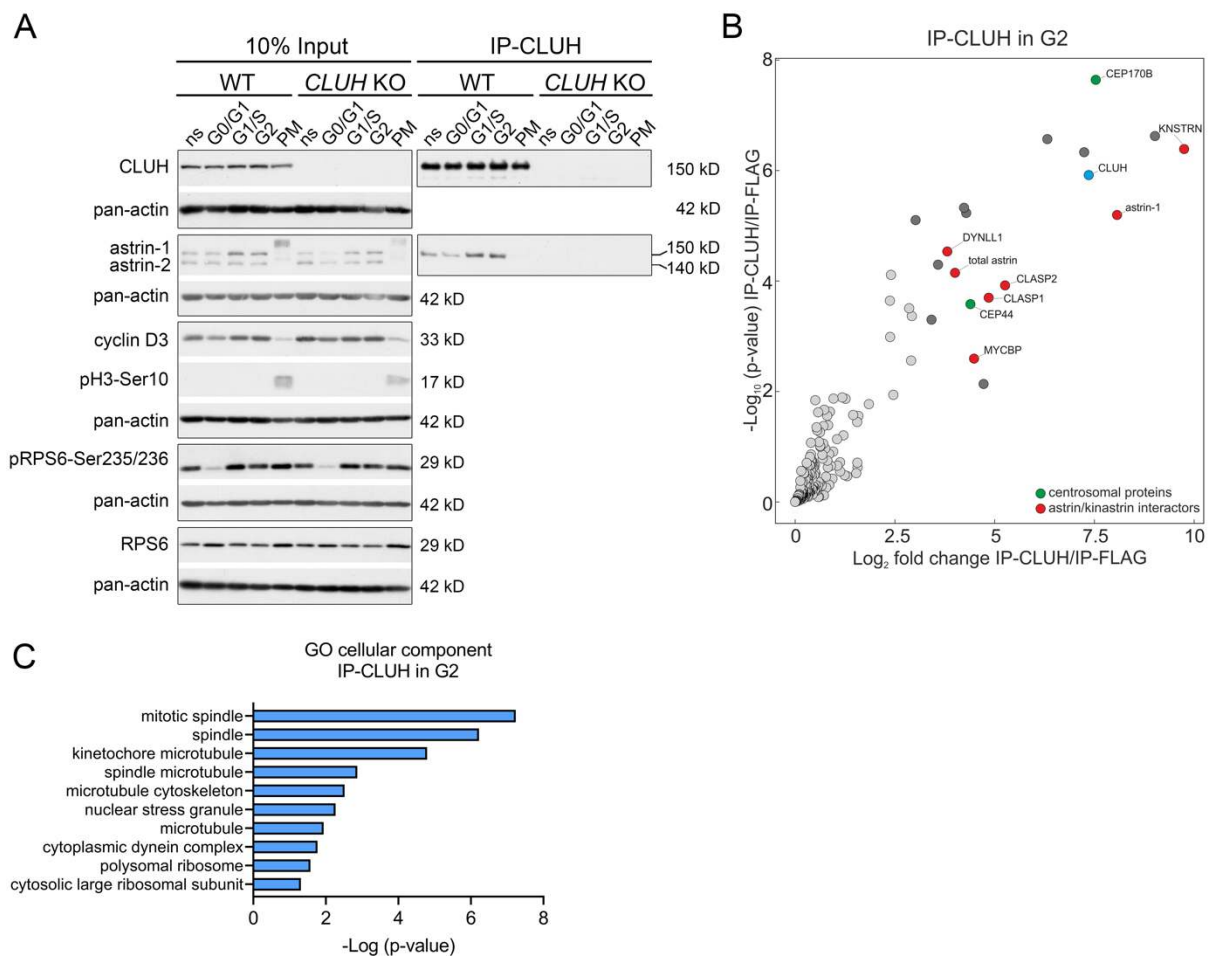
213   **Figure 3. The astrin-1/CLUH complex is enriched in interphase.**

214   (**A**) Western blots of co-IPs of endogenous CLUH in WT and *CLUH* KO HeLa cells. Cells have been

215   synchronized as shown in Figure 3-figure supplement 1A. Pan-actin was used as loading control and

216   cyclin D3 as G2 phase marker, pH3-Ser10 as M phase marker and pRPS6-Ser235/236 to assess effective

217   starvation of input samples. (**B**) Enriched proteins immunoprecipitated with an antibody against

218   endogenous CLUH in G2-synchronized HeLa cells and detected by mass spectrometry (n=4

219   independent replicates). Highlighted are all proteins enriched with a log2FC ≥3 and q≤0.05. Marked in

220   green are centrosomal proteins; marked in red are previously identified astrin/kinastrin interactors. (**C**)

221   GO cellular component analysis of enriched proteins highlighted in B analyzed using the EnrichR

222   webtool.

223

224 To fully capture the CLUH interactome, we performed four biological independent IPs of

225 CLUH in G2-synchronized wildtype cells followed by label-free mass spectrometry (Figure

226 3B, Figure 3-figure supplement 1A). The correct synchronization was confirmed by propidium

227 iodide (PI) staining followed by flow cytometry (Figure 3-figure supplement 1B, C). This

228 experiment confirmed astrin-1 and kinastrin as highly enriched interactors of CLUH (Figure

229 3B and Supplementary Table 2). In addition, proteins previously shown to be part of the

230 astrin/kinastrin complex, such as MYCBP, or linking the complex to the microtubule

231 cytoskeleton were also detected in the precipitate. Among these proteins are CLASP1 and 2,

232 two microtubule plus-end binding proteins, and DYNLL1, a retrograde motor protein (Manning

233 et al, 2010; Schmidt et al, 2010; Dunsch et al, 2011; Kern et al, 2016; Kern et al, 2017) (Figure

234 3B). Interestingly, among top CLUH interactors, we found the centrosomal proteins CEP170B

235 and CEP44, indicating a link of CLUH with the centrosome and the microtubules (Figure 3B,

236 C).

Astrin-1 regulates the subcellular localization of CLUH

238 The previous data strongly indicate the existence of a pool of CLUH that interacts with

239 microtubular structures, including centrosomes. We tested the role of astrin-1 in defining the

240 subcellular localization of CLUH. Overexpression of astrin-1, but not of astrin-2, recruited

241 endogenous CLUH to a perinuclear formation (Figure 4A). These formations are γ-tubulin

242 positive (Figure 4B, C), in line with the reported localization of astrin to the centrosome and

243 the pericentriolar region (Cheng et al, 2007; Thein et al, 2007; Kodani et al, 2015). To

244 substantiate the hypothesis that astrin-1 controls CLUH subcellular localization, we derived a

245 monoclonal cell line completely devoid of astrin expression (referred to as *SPAG5* KO) (Figure

246 4D). CLUH staining was overtly different in these cells, showing a characteristic accumulation

247 in peripheral granular structures in a high percentage of cells (Figure 4E, F). These structures

248 were also positive for vinculin, a marker of focal adhesions (Figure 4E). These findings are

249   consistent with a role of astrin-1 in regulating the localization to the centrosomes of a pool of

250   CLUH.

251
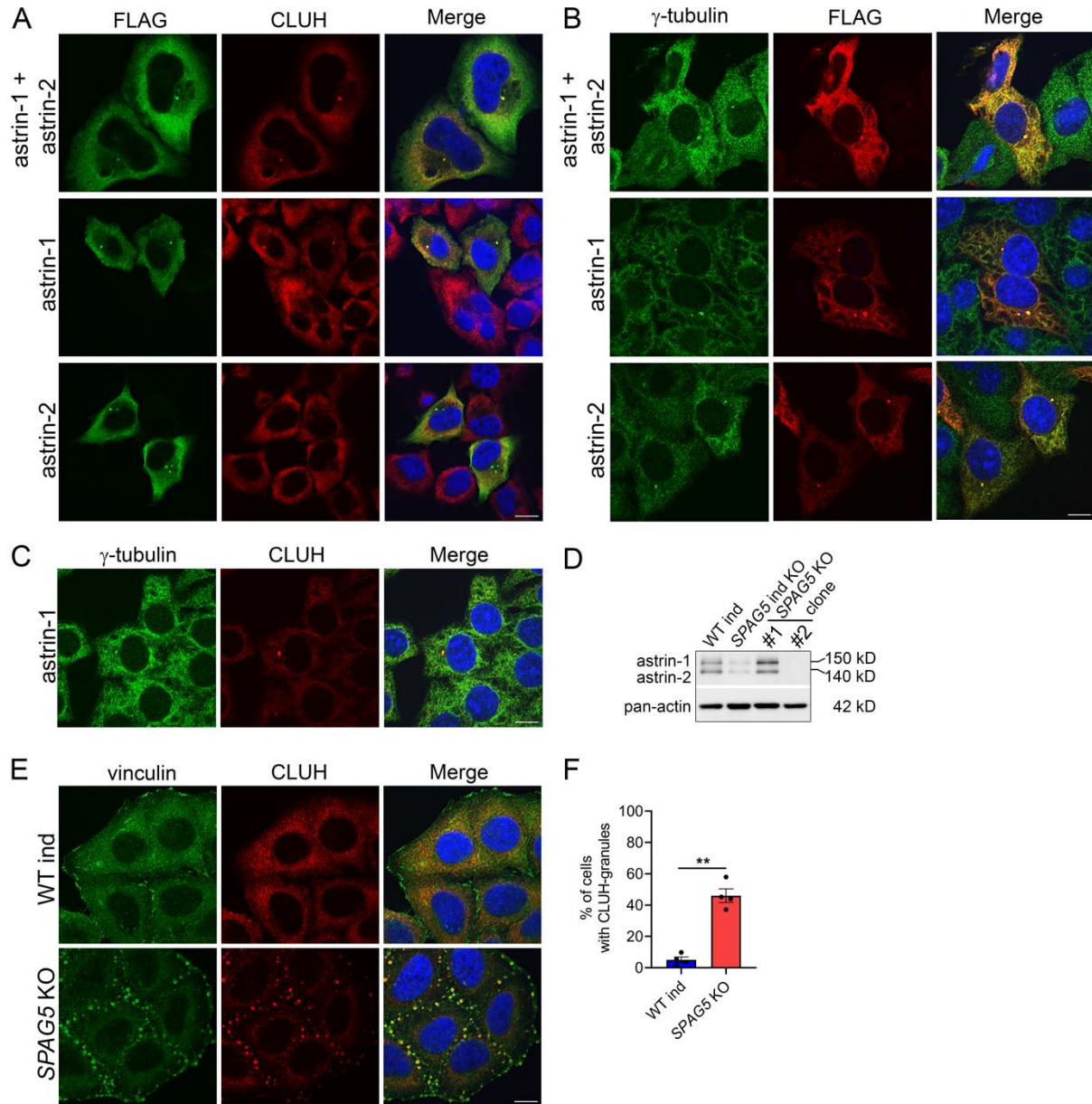
252

253   **Figure 4. Astrin-1 controls CLUH subcellular localization.**

254   (**A-C**) Confocal immunofluorescence pictures of HeLa cells overexpressing FLAG-tagged astrin-1 and

255   astrin-2 (SPAG5), astrin-1 (ATG3+4+5[GGG]-SPAG5) or astrin-2 (ATG1[GGG]-SPAG5) alone stained for

256   FLAG (green) and CLUH (red) (A) or γ-tubulin (green) and FLAG (red) (B) or γ-tubulin (green) and

257   CLUH (red) (C). DAPI was used to stain nuclei (blue). Cells were fixed with 4%PFA/PBS (A) or ice-

258   cold methanol (B, C). Scale bar, 10 μm. (**D**) Western blots of WT and *SPAG5* KO HeLa clones. Pan-

259   actin was used as loading control. *SPAG5* KO clone #2 has been used for experiments in this study. (**E**)

260   Confocal immunofluorescence pictures of WT ind and *SPAG5* KO HeLa cells stained for vinculin

13

261   (green) and CLUH (red). DAPI was used to stain nuclei (blue). Scale bar, 10 µm. (**F**) Quantification of

262   cells with CLUH-granules of experiments as shown in E (n=4 independent experiments). Bars show

263   mean ± SEM and dots represent values of individual replicates. At least 160 cells per genotype per

264   replicate have been counted. Two-tailed paired Student's t-test was performed with P≤0.01: **.

265

266   Loss of astrin or kinastrin do not recapitulate CLUH-dependent

267   mitochondrial phenotypes

268   What is the function of CLUH in complex with astrin-1 and kinastrin? We first asked whether

269   loss of astrin or kinastrin phenocopies CLUH-dependent mitochondrial abnormalities. To avoid

270   possible compensatory effects in stable KO clones, we employed inducible CRISPR-Cas9

271   astrin and kinastrin KO HeLa cells (hereafter referred to as *SPAG5* and *KNSTRN* ind-KO) in

272   which there is constant expression of sgRNAs complementary to the target genes and the

273   expression of the Cas9 is doxycycline inducible (Kern et al, 2017; McKinley & Cheeseman,

274   2017). Using this system, we induced an acute deletion of astrin and kinastrin for four days, in

275   many but not all cells (Figure 5-figure supplement 1A, B). We focused on previously reported

276   phenotypes observed in *CLUH* KO cells or tissues, such as mitochondrial clustering,

277   mitochondrial fragmentation, loss of mtDNA, and decreased assembled respiratory complexes

278   (Gao et al, 2014; Schatton et al, 2017; Wakim et al, 2017). Mitochondrial distribution,

279   morphology, ultrastructure and mtDNA levels were indistinguishable in WT, *SPAG5* and

280   *KNSTRN* ind-KO cells (Figure 5A-C, Figure 5-figure supplement 1C-E). Furthermore,

281   respiratory supercomplexes containing complex I and III assembled normally in these cells, and

282   in-gel activity of complex I was similar to control cells (Figure 5D). In contrast, cells lacking

283   CLUH displayed a reduction of assembled supercomplexes I-III, decreased activity of complex

284   I, and abnormal mitochondrial ultrastructure (Figure 5D and Figure 5-figure supplement 1E).

285   These data indicate that CLUH controls mitochondrial function independent from the

286   interaction with astrin-1 or kinastrin.
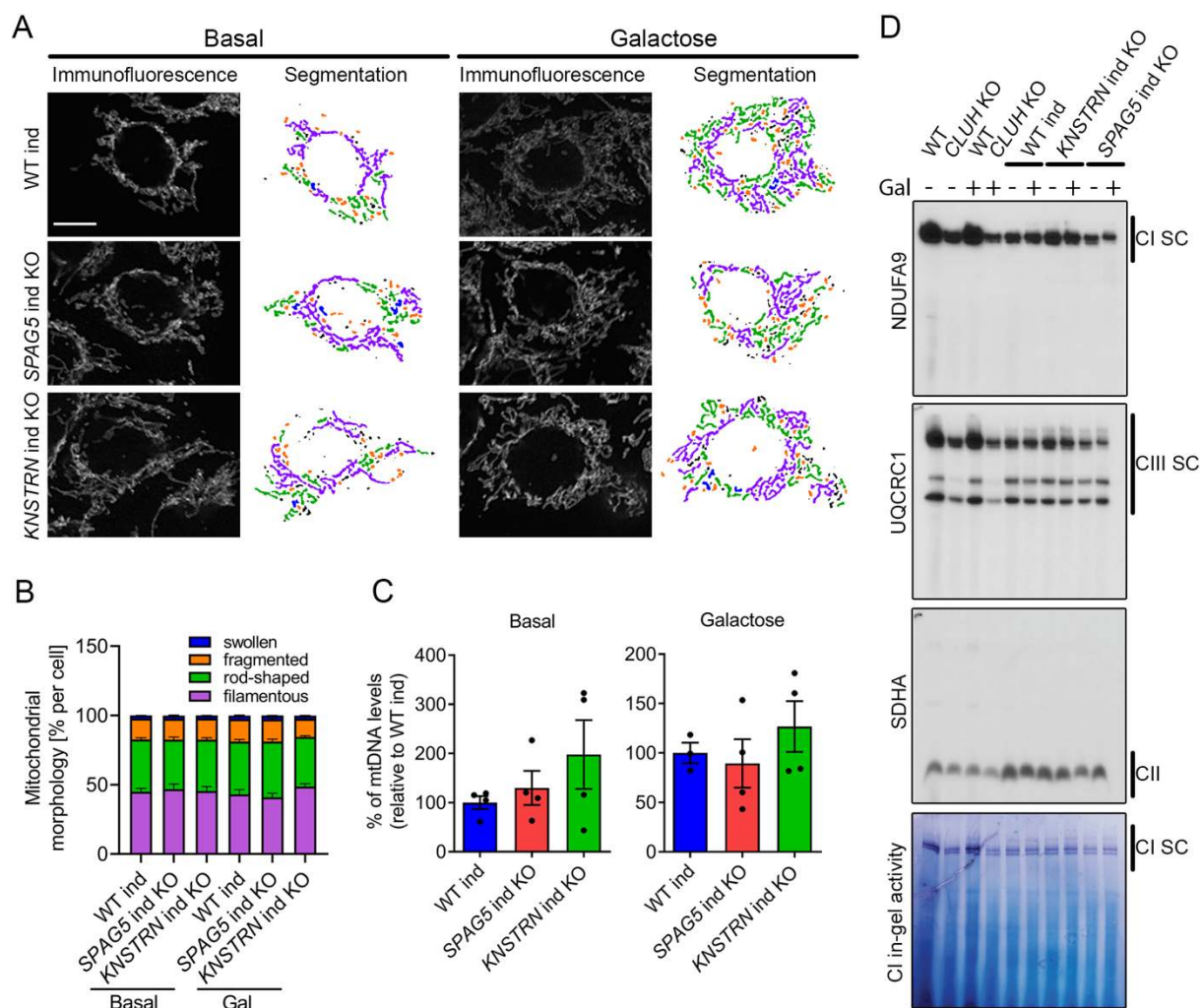
Figure 5. Astrin and kinastrin depletion does not mimic mitochondrial phenotypes seen upon absence of CLUH.

(**A**) Mitochondrial network of WT, *SPAG5* and *KNSTRN* ind-KO HeLa cells grown in basal or galactose media for 16 h. Mitochondria were stained with an antibody against TOMM20. Scale bar, 10 µm. On the left side, confocal immunofluorescence pictures are shown, on the right side, mitochondrial network is shown after segmentation. Color code for different mitochondrial morphologies: purple: filamentous; green: rod-shaped; orange: fragmented; blue: swollen; black: unclassifiable. (**B**) Quantification of mitochondrial morphology of experiments as shown in A (n=3 independent experiments; at least 66 in basal or 44 cells in galactose have been analyzed per genotype per replicate). Bars show the mean of each morphological class with SEM. (**C**) mtDNA levels of WT, *SPAG5* and *KNSTRN* ind-KO HeLa cells grown in basal or galactose media for 16 h (n=4 independent experiments). Bars show mean ± SEM and dots represent values of individual replicates. (**D**) BN-PAGE analysis of respiratory chain supercomplexes and complex I activity staining of isolated mitochondria of WT, *CLUH* KO and WT, *SPAG5* and *KNSTRN* ind-KO HeLa cells grown in basal or galactose media for 16 h.

15

Loss of astrin rewires metabolic pathways to promote anabolism

To define how astrin and kinastrin affect cell function, we performed label free quantitative proteomics in *SPAG5* and *KNSTRN* ind-KO cells. In line with the short time of induced KOs, only minor differences in the overall proteome in *SPAG5* and *KNSTRN* ind-KO cells compared to ind-WT cells was observed (Figure 6A and Supplementary Table 3). Notably, CLUH levels were unaffected by the loss of its interactors (Figure 6A and Supplementary Table 3). Astrin depletion caused a slight decrease of proteins encoded by CLUH mRNA targets (Figure 6A; marked in blue). Downregulated KEGG pathways, analyzed using the EnrichR webtool (using a generous cut-off of $p \leq 0.05$; $q \leq 0.15$) (Chen et al, 2013; Kuleshov et al, 2016; Xie et al, 2021), largely overlapped with metabolic pathways affected by CLUH deletion (TCA cycle, fatty acid and amino acid degradation; Figure 6B) (Schatton et al, 2017). Interestingly, metabolic pathways connected to nucleotide biosynthesis (purine and pyrimidine metabolism), the pentose phosphate pathway (PPP) and glycolysis were upregulated (Figure 6C). Furthermore, mTORC1 appeared as one of the most enriched terms in pathway analysis of perturbed proteins (Figure 6-figure supplement 1A, B).

The proteomic profile of *SPAG5* ind-KO cells is consistent with a previous study that identified astrin as a negative regulator of mTORC1 (Thedieck et al, 2013). We confirmed that mTORC1 is hyperactive in *SPAG5* ind-KOs upon starvation for 8 h in HBSS (Figure 6-figure supplement 1C, D). To reveal if this increased signaling is reflected in cell metabolism, we performed targeted metabolomics analysis in *SPAG5* and *KNSTRN* ind-KO cells.

16

324
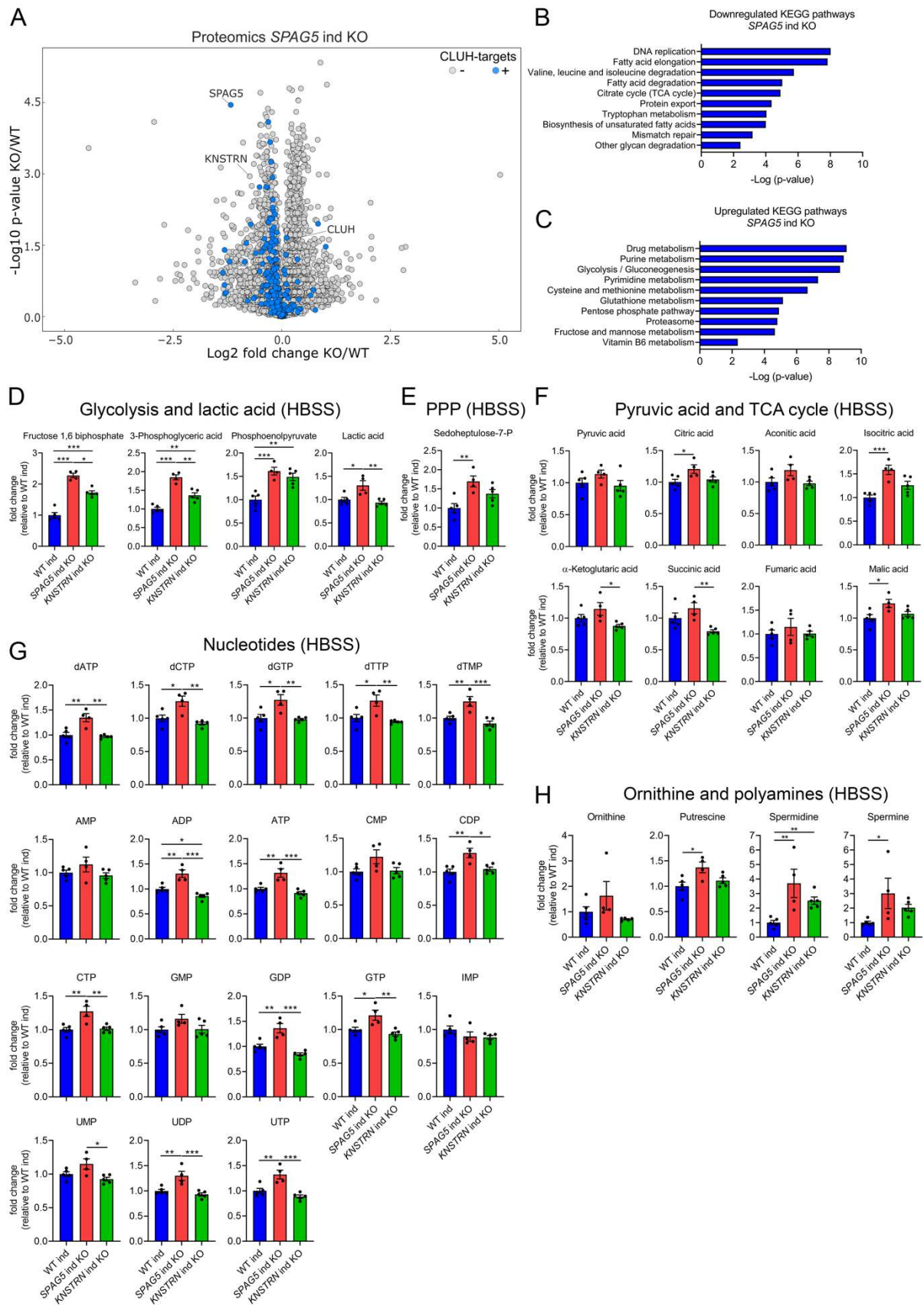
Figure 6. Astrin loss promotes anabolic pathways.

326　(**A**) Volcano plot of label-free proteomics of WT and *SPAG5* ind KO HeLa cells (n=4 independent

327　replicates). CLUH targets are marked in blue. (**B, C**) KEGG pathways of downregulated (B) or

328　upregulated (C) proteins (with a cut-off of p≤0.05; q≤0.15) detected in proteomics analysis of *SPAG5*

329　ind-KO cells (A and Supplementary Table3) using the EnrichR webtool. (**D-H**) Targeted metabolomics

330　of WT, *SPAG5* and *KNSTRN* ind-KO cells after 8 h HBSS starvation showing glycolytic intermediates

331　and lactic acid (D), sedoheptulose-7-P (E), pyruvic acid and TCA cycle intermediates (F), nucleotide

332　levels (G) and ornithine and polyamine levels (H). Bars show mean ± SEM and dots represent values of

333　individual replicates. One-way ANOVA with post hoc Tukey`s multiple comparison tests on log

334　converted fold changes were performed with P≤0.05: *; P≤0.01: **; P≤0.001: ***.

335

336　In agreement with the mild proteomics changes, metabolomics of *SPAG5* ind-KO under basal

337　condition did not reveal major alterations of the pools of glycolytic and TCA cycle

338　intermediates, amino acids, and nucleotides, with the exception of an increase in glutamine,

339　proline, lactate, and citric acid (Figure 6-figure supplement 2A-E). Upon starvation, *SPAG5*

340　depletion led to more prominent alterations of the metabolome, with accumulation of several

341　glycolytic intermediates, lactate, and sedoheptulose-7-phosphate, in agreement with high

342　glycolytic rate and an increase in the PPP (Figure 6D, E). In addition, the TCA cycle

343　intermediates citrate, isocitrate and malate were increased (Figure 6F). Both the TCA cycle and

344　the PPP intermediates are crucial for synthesis of nucleotides, several of which accumulated in

345　astrin-deficient cells (Figure 6G). Amino acid levels were unaffected (Figure 6-figure

346　supplement 2F), with the exception of an increase of ornithine, a precursor of polyamines,

347　which were also more abundant (Figure 6H). *KNSTRN* ind-KO cells did not show detectable

348　metabolic differences to control cells (Figure 6D-H and Figure 6-figure supplement 2A-F).

349　Together, our data show that cells depleted of astrin, despite starvation, engage in anabolic

350　pathways linked to cell growth, in agreement with hyperactivated mTORC1 signaling.

351　**Loss of CLUH impairs anaplerotic and anabolic pathways**

352　Increased mTORC1 signaling upon starvation is also a prerogative of CLUH-deficient cells and

353　tissues (Pla-Martin et al, 2020) (Figure 6-figure supplement 1C, D). Surprisingly, the metabolic

354   profile of starved *CLUH* KO cells was strikingly different from that of *SPAG5* ind-KO cells

355   (Figure 7A-F). Targeted metabolomics revealed a prominent decrease of the PPP intermediate

356   sedoheptulose-7-phosphate, and a significant increase of pyruvate (Figure 7A-C). The

357   intermediates of the first part of the TCA cycle (citrate, aconitate, and isocitrate) were decreased

358   (Figure 7C). In addition, most amino acids that feed into the TCA cycle were decreased (Figure

359   7D), including aspartate, which is mainly produced by oxaloacetate and is an important

360   precursor of pyrimidines (Figure 7D). Glutamine was instead elevated, as well as α-

361   ketoglutarate (Figure 7C, D). In addition, cells lacking CLUH showed a perturbation of

362   polyamines metabolism, with a prominent reduction of spermidine, and decreased levels of

363   some nucleotides, especially inosine monophosphate (IMP), the first nucleotide in the synthesis

364   pathway of purines (Figure 7E, F). Thus, upon starvation *CLUH* KO cells fail to maintain the

365   TCA cycle intermediates (anaplerosis), and surprisingly show defects also in other anabolic

366   pathways that are linked to cell growth and are regulated by mTORC1. This metabolic profile

367   is strikingly opposite to that of *SPAG5* ind-KO cells, and indicate that the mTORC1

368   hyperactivation in absence of CLUH is not reflected in the cellular metabolic rewiring. This

369   data points to an important role of CLUH in the mTORC1-dependent rewiring of cellular

370   metabolism, by supporting mitochondrial anaplerotic pathways.

371
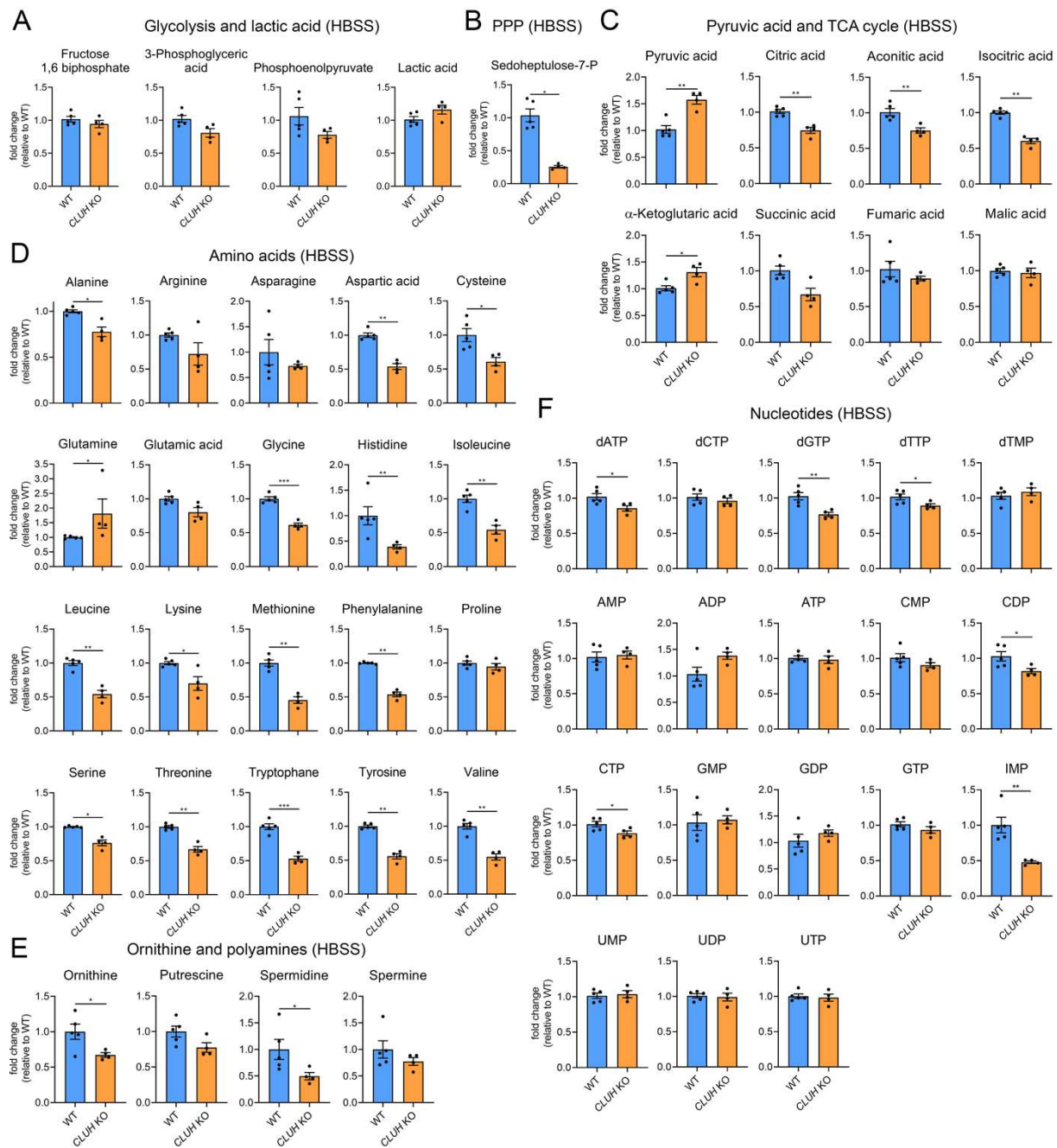
Figure 7. Depletion of CLUH impairs anabolic pathways.

(**A-F**) Targeted metabolomics of WT and *CLUH* KO HeLa cells after 8h HBSS starvation showing glycolytic intermediates and lactic acid (A), sedoheptulose-7-P (B), pyruvic acid and TCA cycle intermediates (C), amino acid levels (D), ornithine and polyamine levels (E) and nucleotide levels (F). Bars show mean ± SEM and dots represent values of individual replicates. Two-tailed unpaired Student`s t-tests on log converted fold changes were performed with $P \leq 0.05$: *; $P \leq 0.01$: **; $P \leq 0.001$: ***.

CLUH controls cell cycle progression

383   In proliferating cells mitochondrial metabolism is constantly adapted to the specific metabolic

385   needs of the different cell cycle phases. Metabolomic analyses during starvation (a treatment

386   that arrests cell proliferation and blocks entry in G2/M) have revealed opposite signatures in

387   cells lacking CLUH or astrin, indicating a perturbed metabolic rewiring. We therefore

388   hypothesized that the functional significance of the interaction of CLUH with astrin and of their

389   reciprocal regulation is to couple mitochondrial metabolism to cell cycle progression. To

390   investigate this possibility, we synchronized wildtype and *CLUH* KO HeLa cells using a double

391   thymidine block (DTB) followed by release for different time points (Figure 8A). To determine

392   the different phases of cell cycle we stained the cells with the DNA dye PI and analyzed them

393   by flow cytometry. *CLUH* KO cells showed different dynamics in cell cycle progression

394   compared to wildtype cells (significant changes in genotype x time in G0/G1, S and G2/M

395   phases; Figure 8B-D). During all time points, slightly more *CLUH* KO cells were in G0/G1

396   phase and less in S and G2/M (Figure 8B-D). Surprisingly, *CLUH* KO cells cycled faster than

397   control cells, with more cells already in G2/M 3 h after the release and more cells entering the

398   next cell cycle at 8 h after release (Figure 8B-E). Consistently, the dynamics of several cell

399   cycle markers was perturbed in *CLUH* KO cells, including precocious phosphorylation of

400   retinoblastoma (p-RB1-Ser807/811) and accumulation of cyclin D3 (Figure 8F). In addition,

401   the inactivating phosphorylation of CDK1 on Tyr15, which occurs in G2 and allows

402   progression into M, showed a different temporal profile (Figure 8F). During G1 the cells double

403   their mass before progressing to M phase and dividing into two daughter cells. *CLUH* KO cells

404   showed a reduced cell size at all time points during the release, in agreement with the defective

405   growth pathways detected by the metabolomics (Figure 8G). Thus, upon loss of CLUH, HeLa

406   cells escape the growth and energy check-point at the end of G1 and proceed faster through the

407   cell cycle. Our results thus identify CLUH as a novel coordinator of mitochondrial activity with

408   the cell cycle progression (Figure 8-figure supplement 1).
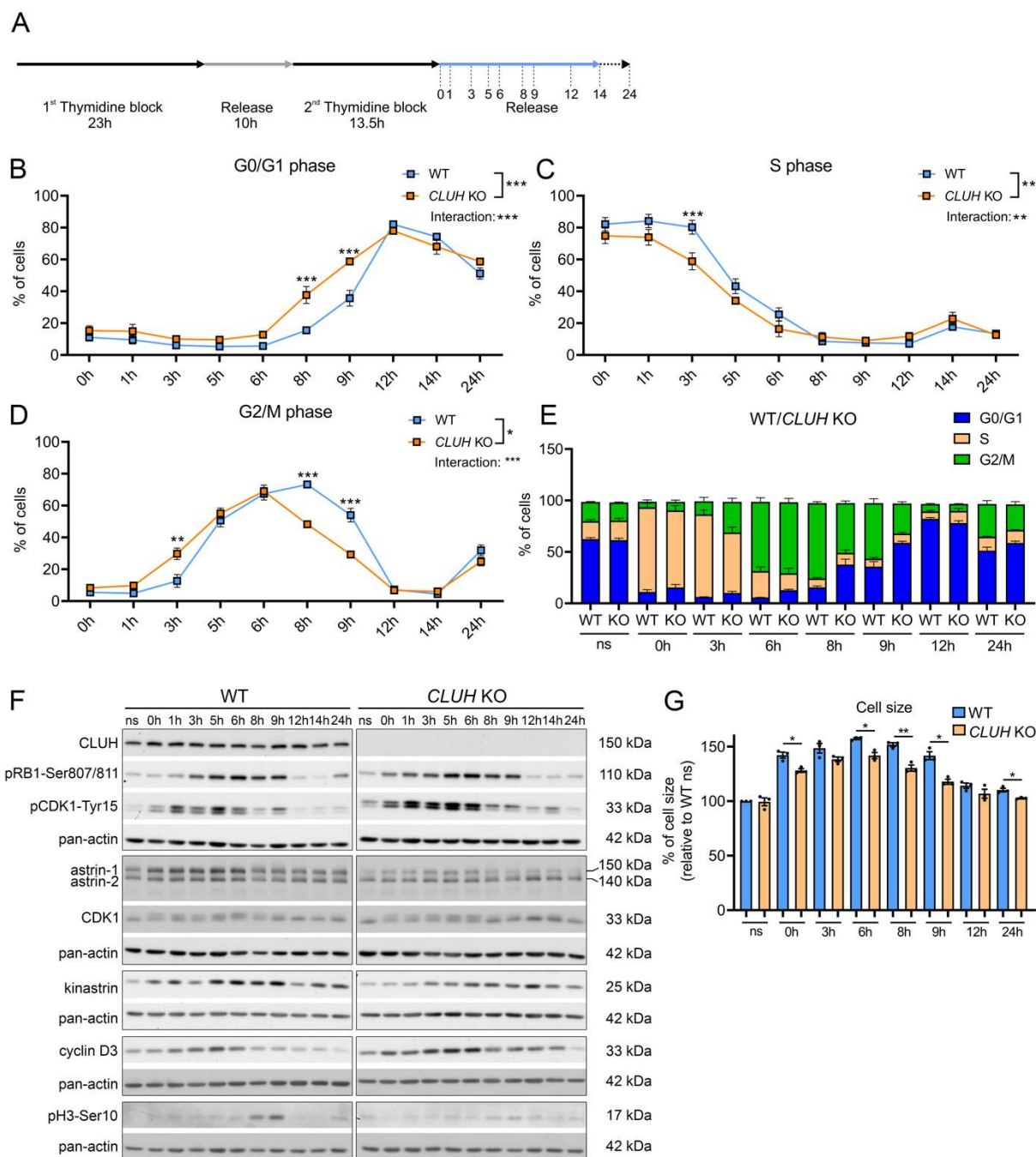
Figure 8. CLUH controls cell cycle progression at the G1/S boundary.

(**A**) DTB synchronization protocol used for cell cycle progression analysis. Cells were collected after release of 2nd thymidine block at indicated time points. (**B-E**) Percentage of WT and *CLUH* KO HeLa cells in G0/G1 (B) in S (C) and G2/M phase (D) and cell cycle distribution analysis (E) after DTB synchronization, collection at indicated time points and PI staining followed by flow cytometric analysis (n=3 independent experiments). For B-D, two-way ANOVA with post hoc Tukey`s multiple comparison tests were performed with $P \leq 0.05$: *; $P \leq 0.01$: **; $P \leq 0.001$: ***. Genotype x time interaction significance is also shown. Graphs and bars show mean ± SEM. (**F**) Western blots of WT and *CLUH* KO HeLa cells collected after

419   DTB synchronization at indicated time points. Pan-actin was used as loading control. (**G**) Cell

420   size analysis of WT and *CLUH* KO HeLa cells of experiments shown in B-E. Bars show mean

421   ± SEM and dots represent values of individual replicates. Two-tailed paired Student`s t-tests

422   were performed with P≤0.05: *; P≤0.01: **.

423

424   **DISCUSSION**

425   We have uncovered a role of CLUH in integrating mitochondrial metabolism with cell cycle

426   progression. Mechanistically, CLUH controls the synthesis and the stability of astrin-1, the full-

427   length protein product of the *SPAG5* gene. Astrin is a coiled-coil protein, with a well-

428   established role during mitosis to stabilize kinetochore-microtubule interactions and allow

429   correct orientation of chromosomes at the metaphase plate (Manning et al, 2010; Dunsch et al,

430   2011; Kern et al, 2017; Ying et al, 2020). Moreover, additional roles of astrin have been

431   reported in interphase, including mTORC1 inhibition (Thedieck et al, 2013), centriole

432   duplication (Kodani et al, 2015), and the recovery from DNA damage at the G2/M transition

433   (Halim et al, 2013). We show here that the interaction of CLUH with astrin is regulated during

434   the cell cycle, and ensures the matching of the mitochondrial metabolic output with the

435   progression of the cell cycle.

436   *SPAG5* upregulation in several cancers has been associated with poor prognosis (Yuan et al,

437   2014; Abdel-Fatah et al, 2016; Bertucci et al, 2016; Zhou et al, 2018; Li et al, 2019). Human

438   cancer cell lines show the expression of two isoforms of astrin, however the origin of these

439   isoforms has not been investigated up to now. We demonstrate that the two astrin isoforms arise

440   by alternative translation initiation, and are regulated by the presence of an uORF and

441   downstream AUGs with good Kozak sequences. Intriguingly, CLUH interacts only with the

442   full-length astrin-1 protein. The N-terminal region of astrin is an unstructured domain that is

443   dispensable for interaction with kinastrin, DYNLL1, MYCBP and the kinetochore (Kern et al,

444   2017). Recently, the PLK1 kinase has been shown to interact with and phosphorylate the astrin

23

445 N-terminus, an important step to stabilize the kinetochore-microtubule attachment (Geraghty

446 et al, 2021). Based on our findings, we speculate that N-terminal phosphorylations are

447 responsible for the lack of interaction of CLUH and astrin-1 in prometaphase. Thus, astrin

448 detaches from CLUH during mitosis when it is required for metaphase to anaphase progression.

449 Interestingly, CLUH appears to regulate astrin-1 expression at multiple levels. The *SPAG5*

450 transcript represents an exception to the finding that mRNAs bound by CLUH mainly encode

451 mitochondrial proteins (Gao et al, 2014). We show here that the *SPAG5* mRNA decays faster

452 and that the synthesis of astrin-1 is impaired in absence of CLUH. It is known that during

453 cytokinesis the E3-ubiquitin ligase MID2 ubiquitinates astrin, targeting it for proteosomal

454 degradation (Gholkar et al, 2016). CLUH may be implicated in supporting synthesis of astrin-

455 1 to replenish its levels in G1. Astrin-1 then accumulates during the S and G2 phases of the cell

456 cycle and is stabilized, together with kinastrin, by binding CLUH.

457 The interaction of CLUH with astrin-1 led us first to investigate the possibility of a role of

458 astrin-1 in concert with CLUH in regulating mitochondrial metabolism. Our data do not support

459 this scenario, since depletion of astrin or kinastrin do not recapitulate the prominent

460 mitochondrial defects observed upon CLUH downregulation or knock-out. Upon loss of astrin

461 or kinastrin, mitochondria are normally dispersed in the cytoplasm, show normal morphology

462 and ultrastructure, do not lose mtDNA and efficiently assemble respiratory supercomplexes.

463 *SPAG5* ind-KO cells showed a mild decrease of the levels of mitochondrial proteins encoded

464 by CLUH target mRNAs. Furthermore, starved cells lacking astrin or CLUH display strikingly

465 opposite metabolic profiles. Finally, astrin and kinastrin are not detected in polysomal fractions,

466 in contrast to CLUH.

467 Our data establish an essential role of CLUH in the metabolic rewiring directed by mTORC1

468 signaling. Upon starvation, both *CLUH* KO and *SPAG5* ind-KO cells showed inappropriate

24

469 mTORC1 activation, in agreement with astrin being a negative regulator of mTORC1

470 (Thedieck et al, 2013). However, the metabolic defects caused by loss of CLUH were

471 discordant with this signaling, with a decrease in the TCA cycle intermediates and in the pool

472 of glycolytic intermediates, some nucleotides, and polyamines. Enzymes of the TCA cycle as

473 well as characteristic anaplerotic enzymes, such as pyruvate carboxylase, proprionyl-CoA

474 carboxylase and other branched amino-acid catabolic enzymes are encoded by *bona fide* CLUH

475 target mRNAs (Gao et al, 2014). These pathways are essential to replenish the TCA cycle

476 intermediates to compensate for their loss upon activation of biosynthetic pathways following

477 mTORC1 signaling. Indeed, a compensatory increase in anaplerotic pathways occurs under

478 conditions of chronic mTORC1 activation (Dutchak et al, 2018). Therefore, CLUH tunes

479 mTORC1 signaling in two independent ways, by regulating the expression of astrin-1 and by

480 ensuring the maintenance of mitochondrial anaplerotic pathways via its RNA-binding function

481 (Figure 8-figure supplement 1). Our data demonstrate another connection between mTORC1

482 signaling and mitochondrial function. mTORC1 positively regulates the translation of

483 mitochondrial proteins involved in oxidative phosphorylation and mitochondrial dynamics

484 (Morita et al, 2013; Morita et al, 2017), while inhibition of mTORC1 activates a lipid signaling

485 cascade that triggers YME1L-mediated intramitochondrial proteolysis to limit mitochondrial

486 biogenesis (MacVicar et al, 2019). Furthermore, mTORC1 hyperactivation is part of the

487 integrated stress response that follows mitochondrial dysfunction (Khan et al, 2017).

488 Proliferating cells must shunt metabolites into mitochondrial pathways that promote cell growth

489 or oxidative respiration and ATP production, depending on the cell cycle phase (DeBerardinis

490 et al, 2008; Salazar-Roa & Malumbres, 2017). In G1 cells double their mass and depend on

491 glycolysis to fuel the TCA cycle and sustain biosynthetic pathways, while in S synthesis of

492 nucleotides is required and glutamine oxidation is prevalent. Interestingly, the TCA cycle

493 intermediates fluctuate during the cell cycle, and it is known that these variations are not

494   transcriptionally regulated (Olsen et al, 2010; Ahn et al, 2017). In mammalian cells, mTORC1

495   activation is important for the transition from G1 to S, an important check point when the energy

496   levels and the growth status of the cell are sensed, and from G2 to M (Cuyàs et al, 2014). We

497   hypothesize that by regulating astrin-1 and stabilizing an RNA regulon involved in the TCA

498   cycle and anaplerotic pathways (Gao et al, 2014), CLUH ensures that the progression of the

499   cell cycle is adjusted with activation of mTORC1 signaling and the mitochondrial metabolic

500   profile (Figure 8-figure supplement 1). Using a post-transcriptional mechanism to coordinate

501   mitochondrial function with cell cycle phases allows a fast and flexible mean to control a broad

502   gene program. Consistently, cells lacking CLUH have cell cycle defects, characterized by a

503   faster cell cycle progression despite failure to properly double the cell mass.

504   Our data not only support a role of CLUH to sustain the mTORC1 signaling cascade, but reveal

505   astrin-1 as a negative regulator of CLUH. Astrin dynamically regulates CLUH subcellular

506   localization: astrin-1 overexpression depletes endogenous CLUH from the cytoplasm and

507   recruits it around the centrosome, while *SPAG5* KO cells show an enrichment of CLUH in

508   structures that contain focal adhesion markers at the plasma membrane. Intriguingly, one study

509   has recently shown that the spatial association of mTORC1 to focal adhesions is not only

510   necessary but also sufficient for the cellular response to growth-promoting signals (Rabanal-

511   Ruiz et al, 2021). Thus, by binding the *SPAG5* mRNA and controlling the stability of astrin-1,

512   CLUH regulates its own subcellular distribution and physiological function. These kinds of

513   feedbacks are commonly operating in metabolic circuits that need to respond to external stimuli,

514   and then recover the original status. It is possible that by sequestering CLUH at the centrosome,

515   astrin-1 puts a break on mTORC1 signaling.

516   More work is needed to characterize the composition and role of the peripheral CLUH

517   structures that we observe upon astrin depletion. Currently, we do not know if these structures

518   contain mRNAs, are translationally active, or recruit mTORC1 components. Moreover, the

519   question arises of the role of CLUH recruitment at the centrosome, which is also strongly

520   supported by the finding of other centrosomal proteins, besides astrin-1, as CLUH molecular

521   partners. Astrin is a component of centriolar satellites in interphase, and it is required for the

522   centrosomal localization of CDK5RAP2, a protein involved in microcephaly, and for proper

523   centriole duplication in S phase (Thein et al, 2007; Kodani et al, 2015), a step which is crucial

524   for cell cycle progression. By recruiting CLUH at the centrosome, astrin may confer a novel

525   signaling role to this organelle, by dynamically relying information on the mitochondrial

526   metabolic status to match it with the progression of the cell cycle. Whether also mRNAs bound

527   to CLUH are recruited to the centrosome is a question to be explored in the future. Finally, our

528   data add to the evidence that astrin plays additional roles outside mitosis. Astrin was also

529   identified in an unbiased screen to be essential for the reentry in mitosis after DNA damage

530   (Halim et al, 2018). This interphase role of astrin should be further explored in view of our

531   findings, as possibly involving dysregulated or enhanced CLUH activity.

532   HeLa cells, as many human cancer cells, overexpress not only astrin-1 but also astrin-2, an

533   isoform of astrin competent to bind all other interactors (kinastrin, DYLNN1 and MYCPB) and

534   the kinetochore (Kern et al, 2017), but not CLUH. We propose that expression of astrin-2

535   endows cancer cells with the ability to proliferate, despite a dysregulated coupling between

536   mitochondrial metabolism and the cell cycle, making CLUH a possible novel therapeutic target

537   in cancers overexpressing *SPAG5*. In conclusions, our findings reveal a novel post-

538   transcriptional mechanism coordinating mitochondrial metabolism and the cell cycle.

539

MATERIAL AND METHODS

Cell lines

HeLa WT and *CLUH* KO cells and immortalized WT and *Cluh* KO MEFs were previously described (Gao et al, 2014; Wakim et al, 2017). Doxycycline inducible CRISPR-Cas9 HeLa WT, *SPAG5* and *KNSTRN* KO cells (Kern et al, 2017; McKinley & Cheeseman, 2017) were kindly provided by Iain Cheeseman (Whitehead Institute for Biomedical Research, Cambridge, USA). To produce inducible HEK293T cells stably expressing 3xFLAG-kinastrin, full length N-terminally 3xFLAG tagged human *KNSTRN* ORF was cloned into pTREx-DEST30 vector by serial Gateway recombinations (Invitrogen) according to the manual. Stable transfected HEK293T cells were generated with the Flp-In T-REx 293 cell system (Invitrogen) following the manual. Positive cells were selected with media containing 1.5 mg/mL hygromycin (InvivoGen) and 150 µg/mL blasticidin (InvivoGen) starting 24h after transfection and single colonies were picked to generate a monoclonal cell line.

Cell culture

All cells were cultured at 37°C and 5% constant CO_2 supply. All cell culture media and ingredients were purchased from Gibco unless stated otherwise. HeLa cells and MEFs were grown in Dulbecco`s modified eagle medium (DMEM) including 4.5 g/L glucose supplemented with 2 mM L-glutamine, 2% penicillin (10,000 u/mL)/ streptomycin (10,000 µg/mL) and 10% FetalClone III serum (Hyclone, Thermo Fisher Scientific). HEK293T cells were cultured in DMEM including 4.5 g/L glucose supplemented with 2 mM L-glutamine, 1 mM sodium pyruvate, 1% nonessential amino acids, 10% tetracycline free fetal bovine serum (Biochrom AG), 1.5 mg/mL hygromycin and 150 µg/mL blasticidin. To induce overexpression, cells were treated with 1 µg/mL tetracycline (Sigma-Aldrich) for 16h. Doxycycline inducible CRISPR-Cas9 HeLa WT, *SPAG5* and *KNSTRN* KO cells were grown in DMEM containing 4.5g/L

566   glucose supplemented with 2 mM L-glutamine, 2% penicillin (10,000 u/mL)/ streptomycin

567   (10,000 μg/mL) and 10% tetracycline free fetal bovine serum (Sigma-Aldrich). To induce Cas9

568   expression, cells were treated with 1 μg/mL doxycycline (Sigma-Aldrich) for four consecutive

569   days adding fresh doxycycline each day. To obtain stable S*PAG5* and *KNSTRN* KO cell lines,

570   induced cells underwent monoclonal selection after serial dilutions.

571

Metabolic labeling

573   For metabolic labelling of newly synthesized astrin, cells were primed in metabolic labeling

574   medium [DMEM containing 4.5 g/L glucose without L-methionine and L-cystine (#21013024,

575   Gibco) including 10% dialysed serum, 2% penicillin (10,000 u/mL)/ streptomycin (10,000

576   μg/mL), 2 mM L-glutamine, 1 mM sodium pyruvate and 1% non-essential amino acids] for 30

577   min followed by incubation with metabolic labeling medium including ^{35}S-methionine (50 μCi

578   per 10 cm plate) for indicated time points.

579

SILAC labeling

581   Cells were cultured in DMEM medium without glutamine, arginine and lysine (Silantes, #

582   280001200), supplemented with 2 mM L-glutamine, 2% penicillin/ streptomycin, dialyzed FCS

583   (Thermofisher, # 26400044), 28 μg/mL L-arginine-HCl (Arg0 or Arg10) (Silantes, #

584   201604102) and 73 μg/mL L-lysine-2HCl (Lys0 or Lys8) (Silantes, # 211604102) for three

585   passages before collecting for IP.

586

CHX chase and galactose treatment

588   To assess protein stability, cells were treated with 0.1 mg/mL CHX (Sigma-Aldrich) with or

589   without 20 μM MG132 (Sigma-Aldrich) for indicated time points. Cells were grown when

590   indicated in galactose media [DMEM, no glucose (#11966-025, Gibco) supplemented with 10

591   mM galactose (Sigma-Aldrich), 2 mM L-glutamine, 1 mM sodium pyruvate, 2% penicillin

29

592   (10,000 u/mL)/ streptomycin (10,000 µg/mL) and 10% dialyzed fetal bovine serum (Gibco)]

593   for 16 h before experiments were performed.

594

Cloning and mutagenesis of SPAG5 constructs

596   The underlying sequence of human *SPAG5* used in this study can be found under the accession

597   number NM_006461.3 on the NCBI database. Human full length *SPAG5* ORF (ATG1-SPAG5)

598   or excluding the first 453 nucleotides (Δ151-SPAG5) were cloned into p3xFLAG-CMV-14

599   (Sigma-Aldrich) using NotI or NotI/ClaI restriction sites, respectively. To obtain a construct

600   including the 5′ UTR (5UTR-SPAG5), the 5′ UTR of *SPAG5* was cloned into Δ151-SPAG5-

601   FLAG using HindIII restriction site. To mutagenize ATGs to GGG, DpnI site directed

602   mutagenesis was employed. Mutagenized base pair positions and construct names are indicated

603   in Figure 1C and S1A.

604

Cell transfection

606   Cells were transfected with Lipofectamine 2000 (Invitrogen) in a plasmid to transfection

607   reagent ratio of 1:5 according to the manual. After 24 h of overexpression, cells were harvested

608   by scraping and pelleting for lysis or fixed with respective reagent for immunofluorescence.

609   RNA interference of *CLUH* was done as described before (Gao et al, 2014). Briefly, HeLa cells

610   were transfected with 100 nM of siRNA against human *CLUH* or control siRNA using

611   Lipofectamine 2000 according to the instructions of the manual and experiments were

612   performed after 72h of downregulation.

613

Polysome profiling

615   Cells were grown in 15 cm dishes to 70-80% confluency and treated for 15 min with fresh

616   media supplied with 100 µg/mL CHX (Sigma Aldrich), followed by crosslinking with 1 mM

617   dithiobis (succinimidyl propionate) (DSP) in PBS for 30 min at RT. prior to polysome profiling

30

618   followed by immunoblotting. Cells were washed with PBS and quenched in 20 mM Tris-HCl,

619   pH 7.4, 5 mM L-cysteine for 10 min. Cells were then washed twice with ice cold PBS

620   containing 100 µg/mL CHX and scraped in 1.5 mL ice cold PBS including CHX and collected

621   in a 2 mL tube. Cells were immediately centrifuged at 21,000 x g for 10 sec at 4°C and

622   supernatant was discarded. Cells were lysed for 30 min on ice in buffer comprised of 20 mM

623   Tris-HCl, pH 7.4, 30 mM KCl, 15 mM MgCl2, 0.5% Triton X-100 (vol/vol), 2 mM DTT, 1

624   mg/mL heparin, 100 µg/mL CHX, 0.16 U/mL RNase inhibitor (RNasin Plus; Promega), and

625   1× EDTA-free protease cocktail (Roche). Cell debris were then removed with 5 min

626   centrifugation at 14 000 x g at 4°C and protein concentration was measured with the standard

627   Bradford assay. Cell lysate was then applied on a continuous 7-47% sucrose gradient (mol

628   weight/volume) in ultra clear tubes (Beckman & Coulter, #331372) and centrifuged at 97,658

629   x g for 3 h at 4°C using a SW41Ti rotor (Beckman & Coulter, # 331362). The polysome

630   fractions were collected using the Foxy R1 Fraction Collector and immediately snap frozen

631   with liquid nitrogen and stored at -80 °C. The polysome profile was detected with the UA-6

632   detector (Teledyne ISCO) during the collection of each polysome fraction.

633

634   **Synchronization of cells**

635   Cells were synchronized by double thymidine block (DTB) using an adapted protocol (Dai et

636   al, 2018). Briefly, cells were plated in desired amount and treated the next day with 2 mM

637   thymidine (Sigma-Aldrich) for 23 h, afterwards cells were released in standard media without

638   thymidine for 10h and second thymidine block (2 mM thymidine) was performed for 13.5 h.

639   Next day, cells were released and collected at indicated time points depending on the

640   experiment (Figure 3-figure supplement 1A, 8A). To enrich cells in PM phase, cells were

641   treated with 100 ng/µl nocodazole (Sigma-Aldrich) after 3 h of release and collected after 12

642   additional hours. To block cells in G0/G1, cells were starved in media without serum for 16h.

643

Immunoprecipitations

For IP cells were collected and lysed in an appropriate volume of IP buffer [50 mM Tris-HCl, pH7.4; 50 mM KCl; 0.1% Triton X-100 supplemented freshly with protease inhibitor cocktail (Sigma-Aldrich)] for 30 min on ice after passing 3x through syringe (30G x 1/2", B. Braun Sterican). For SILAC samples, the lysate was incubated with 25 U benzonase HC nuclease (Sigma-Aldrich) at 37 °C for 30 min before IP. Afterwards, lysates were cleared by centrifugation at 20,000 x g for 30 min and protein amount was determined by standard Bradford assay (Biorad). For each reaction, 300-500 µg of protein were diluted in 250 µl IP buffer and incubated for 3h in head-to-toe agitation at 4°C with 0.5 µg of the specific antibody: rabbit polyclonal rabbit anti-CLUH [#NB100-93305 (1) and #NB100-93306 (2) from Novus Biologicals]; rabbit polyclonal anti-kinastrin (#SAB1103031 from Sigma-Aldrich); rabbit polyclonal anti-astrin (#14726-1-AP from ProteinTech; #NB100-74638 from Novus Biologicals). As control antibodies, we used rabbit polyclonal anti-AFG3L1 (Koppen et al, 2007) (Figure 1A, B and Figure S1C) and rabbit polyclonal anti-FLAG (#F7425 from Sigma-Aldrich) (Figure 3, Figure S1B, D). 20 µl of prewashed magnetic Dynabeads Protein G (Invitrogen) were added per reaction and incubated for 1 h in head-to-toe agitation at 4°C. Afterwards, beads were washed five times with IP buffer. To elute kinastrin, beads were incubated in 100 mM glycine, pH 2.3 for 20 min at 4°C. In the other cases, proteins were eluted in 30 µl 3x Laemmli buffer (20 mM Tris-HCl, pH 6.8, 2% SDS, 5% β-mercaptoethanol, 2.5% glycerol and 2.5% bromophenol blue) by vortexing for 1 min and boiling at 95°C for 5 min. Samples were stored at -20°C or run immediately on SDS-PAGE.

Sample preparation for mass spectrometry

For IP of CLUH followed by mass spectrometry of WT cells enriched in G2, experiments were carried out as described before using 400 µg lysate as input and elution was done with 30 µl SP3 lysis buffer (5% SDS in 1x PBS) by vortexing for 1 min and boiling at 95°C for 5 min.

670   Afterwards, proteins were reduced with 5 mM dithiothreitol for 30 min at 55°C and alkylated

671   with 40 mM chloroacetamide at RT for 30 min in the dark. Next, samples were centrifuged at

672   20,000 x g for 10 min and supernatant was transferred to new tube and stored at -20°C before

673   mass spectrometry was performed. For SILAC labelled samples, beads were resuspended in 50

674   µl of elution buffer 1 (2M urea, 50 mM triethylammoniumbicarbonate, 1 mM DTT, 5 ng/µl

675   trypsin) and incubated at RT for 30 min while shaking. Beads were centrifuged and supernatant

676   transferred to a new tube. Beads were washed twice with elution buffer 2 (2M urea, 50 mM

677   triethylammoniumbicarbonate, 5 mM chloroacetamide) and centrifuged. The eluates were

678   combined. Next, proteins were digested with lysyl endopeptidase (Wako Pure Chemical

679   Industries) and trypsin (Sigma-Aldrich) with an enzyme:substrate ratio of 1:75 at 37 °C for 16

680   h. Next day, samples were acidified with formic acid to stop enzymatic digestion, purified with

681   and loaded on StageTips as described before (Rappsilber et al, 2007).

682   HeLa WT, *SPAG5* and *KNSTRN* ind-KO cells were collected by scraping, pelleted and

683   resuspended in appropriate amount of lysis buffer [50 mM Tris-HCl, pH 7.4; 150 mM NaCl; 1

684   mM EDTA, pH8; 1% IGEPAL CA-630; 0.25% sodium deoxycholate freshly supplemented

685   with protease inhibitor cocktail (Sigma-Aldrich)]. Lysates were passed 3x through syringe (30G

686   x 1/2", B. Braun Sterican) and incubated on ice for 30 min. After centrifugation for 30 min at

687   20,000 x g at 4°C, protein amounts were determined using standard Bradford assay (Biorad)

688   and 30 µg of protein lysate were precipitated with acetone. Briefly, 4x volume of ice-cold

689   acetone were added to lysates, incubated for 15 min at -80°C followed by 90 min incubation at

690   -20°C and centrifugation for 15 min at 16,000 x g. Pellets were washed in ice-cold acetone, air-

691   dried and resuspended in 50 µl of 8 M urea in 50 mM triethylammoniumbicarbonate including

692   protease inhibitor cocktail (Roche). Afterwards proteins were reduced with 5 mM dithiothreitol

693   for 1h at 25°C and alkylated with 40 mM chloroacetamide for 30 min in the dark. Next, proteins

694   were digested with lysyl endopeptidase (Wako Pure Chemical Industries) with an

695   enzyme:substrate ratio of 1:75 at 25°C for 4h. Samples were diluted with 50 mM

696   triethylammoniumbicarbonate to reach a final urea concentration of 2 M. Then proteins were

697   digested with trypsin (Sigma-Aldrich) with an enzyme:substrate ratio of 1:75 and incubation at

698   25°C for 16 h. Next day, samples were acidified with formic acid to stop enzymatic digestion,

699   purified with and loaded on StageTips as described before (Rappsilber et al, 2007). Samples

700   were stored in dried StageTips at 4°C until mass spectrometry was performed.

701

702   **Mass spectrometry of CLUH IP after SILAC**

703   SILAC labelled samples were analyzed on a Q Exactive Plus Orbitrap (Thermo Scientific) mass

704   spectrometer that was coupled to an EASY nLC (Thermo Scientific). Peptides were loaded with

705   solvent A (0.1% formic acid in water) onto an in-house packed analytical column (50 cm x 75

706   µm I.D., filled with 2.7 µm Poroshell EC120 C18, Agilent). Peptides were chromatographically

707   separated at a constant flow rate of 250 nL/min using the following gradient: 7-23% solvent B

708   (0.1% formic acid in 80 % acetonitrile) within 35.0 min, 23-32% solvent B within 5.0 min, 32-

709   85% solvent B within 5.0 min, followed by washing and column equilibration. The mass

710   spectrometer was operated in data-dependent acquisition mode. The MS1 survey scan was

711   acquired from 300-1750 m/z at a resolution of 70,000. The top 10 most abundant peptides were

712   isolated within a 1.8 Th window and subjected to HCD fragmentation at a normalized collision

713   energy of 27%. The AGC target was set to 5e5 charges, allowing a maximum injection time of

714   108 ms. Product ions were detected in the Orbitrap at a resolution of 35,000. Precursors were

715   dynamically excluded for 20.0 s. All mass spectrometric raw data were processed with

716   Maxquant (version 1.5.3.8) using default parameters. Briefly, MS2 spectra were searched

717   against the Uniprot HUMANc_UP000005640.fasta (downloaded at: 26.08.2020) database,

718   including a list of common contaminants. False discovery rates on protein and PSM level were

719   estimated by the target-decoy approach to 1% (Protein FDR) and 1% (PSM FDR) respectively.

720   The minimal peptide length was set to 7 amino acids and carbamidomethylation at cysteine

721   residues was considered as a fixed modification. Oxidation (M) and Acetyl (Protein N-term)

34

722   were included as variable modifications. SILAC/dimethyl labeling quantification was used, and

723   the re-quantify option was enabled.

724

725   **Mass spectrometry of CLUH IP in synchronized cells**

726   Immunoprecipitated proteins from cells synchronized in G2 were analyzed on a Q-Exactive

727   Plus (Thermo Scientific) mass spectrometer that was coupled to an EASY nLC 1200 UPLC

728   (Thermo Scientific). Peptides were loaded with solvent A (0.1% formic acid in water) onto an

729   in-house packed analytical column (50 cm × 75 µm I.D., filled with 2.7 µm Poroshell EC120

730   C18, Agilent). Peptides were chromatographically separated at a constant flow rate of 250

731   nL/min using the following gradient: 3-5% solvent B (0.1% formic acid in 80 % acetonitrile)

732   within 1 min, 5% - 30% solvent B (0.1% formic acid in 80 % acetonitrile) within 40 min, 30%

733   -50% solvent B 8 min and 40% to 95% solvent B within 1 min, followed by washing with 95%

734   solvent B for 10 min. The mass spectrometer was operated in data-dependent acquisition mode.

735   The MS1 survey scan was acquired from 300 to 1750 m/z at a resolution of 70,000. The top 10

736   most abundant peptides were isolated within a 1.8 Th window and subjected to HCD

737   fragmentation at a normalized collision energy of 27%. The AGC target was set to 5e5 charges,

738   allowing a maximum injection time of 110 ms. Product ions were detected in the Orbitrap at a

739   resolution of 35,000. Precursors were dynamically excluded for 10 s. All mass spectrometric

740   raw data were processed with MaxQuant version 1.5.3.8 (Tyanova et al, 2016b) using default

741   parameters. Briefly, MS2 spectra were searched against a canonical Uniprot human fasta

742   database, which was modified by replacing the default entry for SPAG5 (Q96R06) by two

743   separate entries representing (i) the N-terminal 125 amino acids and (ii) the C-terminal

744   sequence from position 126 on. The MaxQuant default list was used to filter for common

745   contaminants. False discovery rates on protein and PSM level were estimated by the target-

746   decoy approach to 1% (Protein FDR) and 1% (PSM FDR) respectively. The minimal peptide

747   length was set to 7 amino acids and carbamidomethylation at cysteine residues was considered

748 as a fixed modification. Oxidation (M) and Acetyl (Protein N-term) were included as variable

749 modifications. The match-between runs option was restricted to replicates of the same

750 condition. LFQ quantification was used with default settings. LFQ intensities were loaded into

751 in Perseus version 1.6.1.1 (Tyanova et al, 2016a). Decoys and potential contaminants were

752 removed and the dataset was filtered for at least 4 out of 4 values in at least one condition.

753 Remaining missing values were imputed with random values from the left end of the intensity

754 distribution using Perseus defaults. Two sample Student's T-test were calculated using

755 permutation-based FDR estimation.

756

757 **Mass spectrometry of *SPAG5* and *KNSTRN* ind-KO cells**

758 For proteomics of HeLa WT ind, *SPAG5* and *KNSTRN* ind-KO cells, peptide digests were

759 analyzed on a Q Exactive plus Orbitrap (Thermo Scientific) mass spectrometer that was coupled

760 to an EASY nLC (Thermo Scientific). Samples were loaded onto an in-house packed analytical

761 column (50 cm x 75 µm I.D., filled with 2.7 µm Poroshell EC120 C18, Agilent). Peptides were

762 separated at a flow rate of 250 nL/min and the following gradient: 3-5% solvent B (0.1% formic

763 acid in 80 % acetonitrile) within 1.0 min, 5-30% solvent B within 91.0 min, 30-50% solvent B

764 within 17.0 min, 50-95% solvent B within 1.0 min, followed by washing with 95 % solvent B

765 for 10 min. DDA runs for spectrum library generation were acquired from distinct pools of the

766 sample groups and Hek293 cell digests fractionated high pH HPLC. MS1 survey scan were

767 acquired at a resolution of 70,000. The top 10 most abundant peptides were isolated within a

768 2.0 Th window and subjected to HCD fragmentation with normalized collision energy of 27%.

769 The AGC target was set to 5e5 charges, allowing a maximum injection time of 105 ms. Product

770 ions were detected in the orbitrap at a resolution of 35,000. Precursors were dynamically

771 excluded for 20.0 s. Sample runs were acquired in data-independent mode using 10 variable

772 windows covering the mass range from m/z 450 to m/z 1200. MS1 scans were acquired at

773 140,000 resolution, maximum IT restricted to 120 ms and an AGC target set to 5e6 charges.

774 The settings for MS2 scans were 17,500 resolution, maximum IT restricted to 60 ms and AGC

775 target set to 5e6 charges. The default charge state for the MS2 was set to 4. Stepped normalized

776 collision energy was set to 23.5, 26 and 28.5. All spectra were acquired in profile mode. A

777 hybrid spectrum library was generated in Spectronaut 13 (Bruderer et al, 2015) using DDA

778 library runs, DIA sample runs and a canonical human sequence file (SwissProt, 20416 entries)

779 downloaded from Uniprot. Spectronaut default settings were used for the analysis of the DIA

780 runs. Protein identifications were filtered for q-values below 0.01 and normalized intensities

781 were exported for subsequent statistical analysis in Perseus 1.6.1.1 (Tyanova et al, 2016b).

782 Intensities were transformed to log2 values and the dataset was filtered for at least 4 out of 4

783 values in at least one condition. Remaining missing values were imputed with random values

784 from the left end of the intensity distribution (with 0.3 sd, downshift 2 sd). Two sample

785 Student´s T-tests were calculated using permutation based FDR estimation.

786

787 **Proteomics visualization and pathway analysis**

788 Enriched proteins of IP experiment or proteomics results were visualized as volcano plots using

789 Instant Clue software (Nolte et al, 2018) and pathway analysis was carried out using the

790 EnrichR webtool with a cut off of q≤0.05 and log2 fold change ≥ 3 for the IP and a cut off of

791 q≤0.15 and p≤0.05 for the proteomics analysis (Chen et al, 2013; Kuleshov et al, 2016; Xie et

792 al, 2021).

793

794 **Isolation of mitochondria**

795 Cells were collected from confluent 15 cm plates with trypsinization, washed twice with PBS,

796 and resuspended in an ice-cold mitochondria isolation buffer containing 20 mM HEPES, pH

797 7.6; 220 mM mannitol; 70 mM sucrose; 1 mM EDTA; 0.2% fatty acid-free bovine serum

798 albumin (BSA). After 20 min of incubation on ice, cells were homogenized using the rotational

799 engine homogenizer (Potter S, Sartorius; 30 strokes, 1200 rpm) followed by centrifugation at

800   850 × g. Next, mitochondria were pelleted at 8500 × g for 10 min at 4 °C, washed with BSA-

801   free buffer, and protein concentration was determined with Bradford reagent (Sigma-Aldrich).

802   For further analysis, mitochondria were subjected to blue native polyacrylamide gel

803   electrophoresis (BN-PAGE) followed by western blotting or determination of the in-

804   gel activity of respiratory complexes

805

806   **Analysis of mitochondrial respiratory complexes with BN-PAGE**

807   20 mg of mitochondria were lysed with digitonin (Calbiochem; 6.6 g/g protein) for 15 min on

808   ice with occasional vortexing and cleared from insoluble material for 20 min at 20,000 × g at 4

809   °C. Lysates were combined with Coomassie G-250 (0.25% final concentration). Mitochondrial

810   respiratory supercomplexes were resolved with BN-PAGE using the 4–16% NativePAGE

811   Novex Bis-Tris Mini Gels (Invitrogen) in a Bis-Tris/Tricine buffering system with cathode

812   buffer initially supplemented with 0.02% G-250 followed by the 0.002% G-250. For complex

813   I in-gel activity, gels were incubated at RT in a buffer containing 0.01 mg/mL NADH and 2.5

814   mg/mL nitrotetrazolium blue in 5 mM Tris-HCl, pH 7.4.

815   **Cell lysis and western blot**

816   Cell pellets were lysed in appropriate amount of lysis buffer [50 mM Tris-HCl, pH 7.4; 150

817   mM NaCl; 1 mM EDTA, pH8; 1% IGEPAL CA-630; 0.25% sodium deoxycholate freshly

818   supplemented with protease inhibitor cocktail (Sigma-Aldrich)] and protein amounts were

819   determined by standard Bradford assay (Biorad). Desired protein amounts were mixed with

820   appropriate volume of 3x loading buffer (20 mM Tris-HCl, pH6.8; 2% SDS; 5% β-

821   mercaptoethanol; 2.5% glycerol and 2.5% bromophenol blue), boiled for 5 min at 95°C and

822   loaded on SDS polyacrylamide gels. Proteins were separated by SDS PAGE and blotted on

823   polyvinylidene fluoride (PVDF) membranes using wet transfer. After BN-PAGE, separated

824   mitochondrial complexes were transferred on PVDF membranes using the wet transfer sodium

825　lauryl sulfate (SDS)-free and methanol-free system. The following primary antibodies were

826　used for western blotting: rabbit polyclonal anti-CLUH antibodies [detecting human CLUH;

827　#NB100-93305 (1), #NB100-93306 (2)], rabbit polyclonal anti-RPS6 (#NB100-1595), rabbit

828　polyclonal anti-RPL7 (#NB100-2269) antibodies from Novus Biologicals; rabbit polyclonal

829　anti-astrin (#14726-1-AP) antibody from ProteinTech; rabbit polyclonal anti-FLAG (#F7425)

830　and mouse monoclonal anti-FLAG (#F3165) antibodies from Sigma-Aldrich; mouse

831　monoclonal pan-actin (#MAB1501) and anti-GAPDH (#MAB374) antibodies from EMD

832　Millipore; rabbit polyclonal anti-CLUH antibody (detecting murine CLUH;

833　#ARP70642_P050) from Aviva; rabbit polyclonal anti-kinastrin (#ab122769) and rabbit

834　polyclonal pH3-Ser10 (#ab5176) antibodies from Abcam; mouse monoclonal anti-SDHA

835　(#459200), anti-NDUFA9 (#459100) and anti-UQCRC1 (#459140) from Molecular probes;

836　rabbit polyclonal pRB1-Ser807/811 (#9308), rabbit monoclonal pCDK1-Tyr15 (#4539), mouse

837　monoclonal anti-cyclin D3 (#2936) and rabbit polyclonal pRPS6-Ser235/236 (#2211)

838　antibodies from Cell Signaling and mouse monoclonal anti-CDK1 (#sc-54) antibody from

839　Santa Cruz Biotechnologies.

840

841　**Sample collection to measure anionic metabolites, amino acids and polyamines**

842　WT, *SPAG5* and *KNSTRN* ind-KO cells were induced as described before and 1,000,000 cells

843　were plated in 6 well plates the day before the extraction. Next day, the cells were either

844　collected immediately (basal condition) or starved for 8h in HBSS media (#14025092, Gibco)

845　in absence of doxycycline. Cells were washed twice with buffer containing 75 mM ammonium

846　carbonate (pH7.4) and metabolites were extracted with cold (-20°C) extraction solvent

847　(40:40:20 acetonitrile:methanol:water) and incubation for 10 min at -20°C. Supernatant was

848　collected and extraction was repeated. Afterwards, cells were scraped on ice and combined with

849　the supernatant of the previous step. Samples were immediately dried in a speed vac

850　concentrator and dried pellets were kept at -80°C until mass spectrometry was performed.

851

Anion-Exchange Chromatography Mass Spectrometry (AEX-MS) for the analysis of

anionic metabolites

Extracted metabolites were re-suspended in 150 µl of Optima LC/MS grade water (Thermo

Fisher Scientific), of which 100 µl were transferred to polypropylene autosampler vials

(Chromatography Accessories Trott, Germany) before AEX MS analysis. The samples were

analysed using a Dionex ionchromatography system (Integrion, Thermo Fisher Scientific) as

described previously (Schwaiger et al, 2017). In brief, 5 µL of polar metabolite extract were

injected in push partial mode using an overfill factor of 3, onto a Dionex IonPac AS11-HC

column (2 mm × 250 mm, 4 µm particle size, Thermo Fisher Scientific) equipped with a Dionex

IonPac AG11-HC guard column (2 mm × 50 mm, 4 µm, Thermo Fisher Scientific). The column

temperature was held at 30°C, while the auto sampler was set to 6°C. A potassium hydroxide

gradient was generated using a potassium hydroxide cartridge (Eluent Generator, Thermo

Scientific), which was supplied with deionized water. The metabolite separation was carried at

a flow rate of 380 µL/min, applying the following gradient conditions: 0-3 min, 10 mM KOH;

3-12 min, 10-50 mM KOH; 12-19 min, 50-100 mM KOH, 19-21 min, 100 mM KOH, 21-22

min, 100-10 mM KOH. The column was re-equilibrated at 10 mM for 8 min. For the analysis

of metabolic pool sizes the eluting compounds were detected in negative ion mode $[M-H]^-$ using

multiple reaction monitoring (MRM) mode with the following settings: Capillary voltage 2.7

kV, desolvation temperature 550°C, desolvation gas flow 800 l/h, collision cell gas flow 0.15

mL/min. The detailed quantitative and qualitative transitions and electronic settings for the

analyzed metabolites are summarized in Supplementary Table 4. The MS data analysis was

performed using the TargetLynx Software (Version 4.1, Waters). For data analysis the area of

the quantitative transition of each compound was extracted and integrated using a retention time

(RT) tolerance of <0.1 min as compared to the independently measured reference compounds.

Areas of the cellular pool sizes were normalized to the internal standards (citric acid D4), which

877   were added to the extraction buffer, followed by a normalization to the protein content of the

878   analyzed sample. One sample of *CLUH* KO and one of *SPAG5* ind-KO cells upon HBSS

879   starvation has been classified as outlier and removed from analysis. Samples were classified as

880   outliers due to PCA plot and tremendous drift of measured values from other samples.

881

882   **LC-MS analysis of cellular pool sizes of amino acids and polyamines**

883   For amino acid analysis, the benzoylchlorid derivatization method (Wong et al, 2016) was used.

884   In brief, 20 µl of the polar phase of each sample, were mixed with 10 µl of 100 mM sodium

885   carbonate (Sigma-Aldrich) followed by the addition of 10 µl 2% benzoylchloride (Sigma-

886   Aldrich) in acetonitrile (VWR). Samples were analyzed using an Acquity iClass UPLC

887   (Waters) connected to a Q-Exactive HF (Thermo Fisher Scientific). For analysis, 1 µl of the

888   derivatized sample was injected onto a 100 x 1.0 mm HSS T3 column, packed with 1.8 µm

889   particles (Waters). The flow rate was 100 µL/min and the buffer system consisted of buffer A

890   (10 mM ammonium formate, 0.15% formic acid in water) and buffer B (acetonitrile). The

891   gradient was: 0% B at 0 min; 0-15% B 0-0.1 min; 15-17% B 0.1-0.5 min; 17-55% B 0.5-14

892   min, 55-70% B 14-14.5 min; 70-100% B 14.5-18 min; 100% B 18-19 min; 100-0% B 19-19.1

893   min, 19.1-28 min 0% B. The mass spectrometer was operating in positive ionization mode

894   monitoring and the mass range was set to m/z 50-750. The heated ESI source settings of the

895   mass spectrometer were: Spray voltage 3.5kV, capillary temperature 275°C, sheath gas flow 40

896   AU and aux gas flow 20 AU at a temperature of 300°C. The S-lens was set to 60 AU. Data

897   analysis was performed using the TraceFinder software (Version 4.1, Thermo Fisher

898   Scientific). Identity of each compound was validated by authentic reference compounds, which

899   were injected and analyzed independently. Extracted ion chromatograms (XIC) were extracted

900   as $[M + H]^+$ ions with a mass accuracy (<5 ppm). Areas of the cellular pool sizes of the analyzed

901   amines were normalized to their corresponding $^{13}C^{15}N$ internal standard or, if no corresponding

902     $^{13}C^{15}N$ compound was present, they were normalized to the $^{13}C^{15}N$ leucine. Following the

41

903   normalization to the internal standard the values were normalized to the protein content of the

904   analyzed sample.

905

906   **Measurement of RNA stability**

907   To measure mRNA stability, Click-iT Nascent RNA Capture Kit (Invitrogen) was used as

908   described before (Schatton et al., 2017). Briefly, 500,000 cells were seeded on 3.5 cm dishes.

909   The following day, endogenous RNA was labeled with 0.2 mM 5-ethynyl uridine (EU) for 24h

910   and collected either immediately (0h time point) or after 8h incubation with media w/o EU with

911   Trizol reagent (Invitrogen). Total RNA was isolated according to the instructions of the Trizol

912   reagent manual and 3 µg RNA were biotinylated with biotin-azide using Click-iT chemistry

913   reaction. Afterwards, RNA was precipitated with glycogen, 7.5 M ammonium acetate and

914   100% ice cold ethanol for 16h and centrifugation at 13,000 x g for 20 min at 4°C. RNA was

915   washed twice with 70% ethanol, air-dried and resuspended in distilled H2O. 1.5 µg RNA were

916   incubated with prewashed Dynabeads MyOne Streptavidin T1 beads (Invitrogen) for 30 min in

917   presence of RNaseOUT (Invitrogen). Afterwards beads were washed several times and RNA

918   bound on beads was retrotranscribed with SuperScript VILO cDNA synthesis kit (Invitrogen)

919   according to the manual. cDNA was stored at -20°C until qRT-PCR was performed. mRNA

920   half-lives were calculated as described before (Schatton et al, 2017).

921

922   **RNA isolation, cDNA synthesis, DNA isolation and quantitative real-time PCR**

923   RNA was isolated with Trizol reagent (Invitrogen) according to the manual. 2 µg of total RNA

924   were retro-transcribed using the SuperScript First-Strand Synthesis System (Invitrogen) with

925   random hexamer primers according to the instructions of the manual. To isolate genomic DNA,

926   cells were lysed with digestion buffer [100 mM NaCl; 10 mM Tris-HCl, pH8; 25 mM EDTA,

927   pH8; 0.5% SDS supplemented freshly with 0.1 mg/mL proteinase K (Roche)] at 55°C for 16h.

928   DNA was isolated with standard phenol/chloroform purification followed by ethanol

929 precipitation. For mtDNA quantification, 20 ng genomic DNA were used per reaction. SYBR

930 green master mix (Applied Biosystems) was used for quantitative real-time PCR using either

931 StepOne Plus Real-Time PCR system or Quant Studio 12K Flex Real-Time PCR Sytem

932 thermocycler (Applied Biosystems). For each reaction technical duplicates and at least three

933 biological replicates per experiment were performed. *GAPDH* or *RPL13* were used for

934 normalization and fold enrichment was calculated with the formula: $2^{(-\Delta\Delta Ct)}$. The following

935 primers were used for amplification: *SPAG5* forward: 5'-

936 CATCTCACAGTGGGATAACTAATAAAC-3'; *SPAG5* reverse: 5'-

937 CAGGGATAGGTGAAGCAAGGATA-3'; *GAPDH* forward: 5'-

938 AATCCCATCACCATCTTCCA-3'; *GAPDH* reverse: 5'-TGGACTCCACGACGTACTCA-3';

939 *RPL13* forward: 5'-CGGACCGTGCGAGGTAT-3'; *RPL13* reverse: 5'-

940 CACCATCCGCTTTTTCTTGTC-3'; *MT-TL1* forward: 5'-CACCCAAGAACAGGGTTTGT-

941 3'; *MT-TL1* reverse: 5'-TGGCCATGGGTATGTTGTTA-3'; *B2M* forward: 5'-

942 TGCTGTCTCCATGTTTGATGTATCT-3'; *B2M* reverse: 5'-

943 TCTCTGCTCCCCACCTCTAAGT-3'.

944

945 **Immunofluorescence and transmission electron microscopy**

946 Cells were seeded in an appropriate amount on coverslips the day before. Next day, cells were

947 washed twice with 1x PBS and fixed for 15 min either with 4% PFA/PBS (pH7.4) or with ice-

948 cold 100% methanol at RT or -20°C, respectively, depending on the primary antibody and as

949 indicated in the figure legends. Afterwards, cells were permeabilized with 0.2% Triton X-100

950 in 1x PBS for 10 min and blocked in 10% pig or goat serum for 10 min. Then coverslips were

951 stained with primary antibodies diluted in 1% pig or goat serum in 1x PBS for 2h at RT or for

952 16h at 4°C. The following primary antibodies were used: rabbit polyclonal anti-CLUH antibody

953 (1:1000, #NB100-93306, Novus Biologicals), mouse monoclonal anti-FLAG antibody (1:1000,

954 #F3165, Sigma-Aldrich), mouse monoclonal anti-vinculin antibody (1:500, #MAB3574, EMD

955 Millipore), mouse monoclonal anti-TOMM20 antibody (1:1000, #sc-17764, Santa Cruz

956 Biotechnologies), mouse monoclonal anti-γ-tubulin antibody (1:1000, #T6557, Sigma-Aldrich)

957 and rabbit polyclonal anti-FLAG antibody (1:1000, #F7425, Sigma-Aldrich). Afterwards,

958 coverslips were washed three times in 1x PBS for 5 min and incubated with secondary

959 antibodies [donkey anti-rabbit Alexa594 (1:1000, #A21207, Invitrogen) and goat anti-mouse

960 Alexa488 (1:1000, #11029, Invitrogen)] diluted in 1x PBS including 1% pig or goat serum for

961 1h at RT. Then coverslips were washed 3x in 1x PBS (the first washing including DAPI DNA

962 dye) and mounted with Fluorsave reagent (Calibiochem). Transmission electron microscopy on

963 cells was performed as previously described (Gao et al, 2014).

964

965 **Microscopy and image analysis**

966 Immunofluorescence images were acquired with a spinning-disk confocal microscope

967 (UltraVIEW VoX, PerkinElmer) using a 60× objective. Images represent a single plane and

968 were deconvoluted using ImageJ (NIH) and brightness was adjusted equally in the entire

969 images. Specificity of the anti-CLUH antibody has been proven before (Pla-Martin et al, 2020).

970 For CLUH-granule quantification, at least 160 cells have been analyzed per genotype per

971 experiment and cells with CLUH-granules were counted manually with the experimentator

972 blinded for the genotype. For mitochondrial morphology assessment, a half-automated macro

973 for ImageJ (Mitomorph) has been employed (Yim et al, 2020). At least 66 (basal) or 44

974 (galactose) cells per genotype per experiment were analyzed. Micrographs were acquired on a

975 Jeol Jem2100Plus electron microscope operating at a voltage of 120 V using a GATAN

976 OneView camera.

977

978 **Propidium iodide staining and flow cytometry**

979 Cells were synchronized as described before (Figure 8A), collected by trypsinization and

980 pelleting, washed once with 1x PBS, fixed in ice-cold 70% ethanol in 1x PBS and stored at -

981   20°C for at least 16h. Fixed cells were pelleted at 2000 rpm for 10 min, washed once with 1x

982   PBS and pelleted again at 2000 rpm for 5 min. Pellets were resuspended in 500 µl 1x PBS

983   containing 0.25% Triton X-100, 100 µg/mL RNase A (#1007885, Qiagen) and 50 µg/mL PI

984   (#P4864, Sigma-Aldrich) and incubated at least 30 min at RT before measured by flow

985   cytometry. BD LSR Fortessa (BD Biosciences) was used with BD FACS Diva software at low

986   flow rate using PE laser (561 nm excitation; 586/15 nm detection). At least 15,000 events were

987   measured per sample. Flowing Software version 2.5.1 (developed by Perttu Terho, Turku

988   Centre for Biotechnology, University of Turku, Finland) was used for analysis.

989   **Statistics**

990   Sample size has been determined by previous experience with similar analysis. Replicates are

991   always biological independent experiments. Data are shown as mean ± SEM or ± SD as

992   indicated in respective figure legends. To compare two groups, paired or unpaired Student`s t-

993   test was performed as indicated in the figure legends. To compare multiple groups, one-way

994   ANOVA with post hoc Tukey`s multiple comparison test was performed. To compare data sets

995   including two variances, two-way ANOVA with post hoc Tukey's multiple comparison test

996   was employed. Statistical significance was calculated using GraphPad Prism software. A P

997   value < 0.05 was considered as significant. Statistical methods for proteomics analysis are

998   described in the corresponding method section.

999

1007
1008
1009 **COMPETING INTERESTS**

1010 The authors declare no competing interests.

1011

1012 **REFERENCES**

1013 Abdel-Fatah TMA, Agarwal D, Liu DX, Russell R, Rueda OM, Liu K, Xu B, Moseley PM, Green AR,
1014 Pockley AG, Rees RC, Caldas C, Ellis IO, Ball GR, Chan SYT (2016) SPAG5 as a prognostic biomarker
1015 and chemotherapy sensitivity predictor in breast cancer: a retrospective, integrated genomic,
1016 transcriptomic, and protein analysis. *Lancet Oncol* **17:** 1004-1018

1017
1018 Ahn E, Kumar P, Mukha D, Tzur A, Shlomi T (2017) Temporal fluxomics reveals oscillations in TCA
1019 cycle flux throughout the mammalian cell cycle. *Molecular Systems Biology* **13:** 953

1020
1021 Bertucci F, Viens P, Birnbaum D (2016) SPAG5: the ultimate marker of proliferation in early breast
1022 cancer? *Lancet Oncol* **17:** 863-865

1023
1024 Bruderer R, Bernhardt OM, Gandhi T, Miladinović SM, Cheng LY, Messner S, Ehrenberger T, Zanotelli
1025 V, Butscheid Y, Escher C, Vitek O, Rinner O, Reiter L (2015) Extending the limits of quantitative
1026 proteome profiling with data-independent acquisition and application to acetaminophen-treated three-
1027 dimensional liver microtissues. *Mol Cell Proteomics* **14:** 1400-1410

1028
1029 Buchakjian MR, Kornbluth S (2010) The engine driving the ship: metabolic steering of cell proliferation
1030 and death. *Nat Rev Mol Cell Bio* **11:** 715-727

1031
1032 Chang MS, Huang CJ, Chen ML, Chen ST, Fan CC, Chu JM, Lin WC, Yang YC (2001) Cloning and
1033 characterization of hMAP126, a new member of mitotic spindle-associated proteins. *Biochem Biophys
1034 Res Commun* **287:** 116-121

1035
1036 Chen EY, Tan CM, Kou Y, Duan Q, Wang Z, Meirelles GV, Clark NR, Ma'ayan A (2013) Enrichr:
1037 interactive and collaborative HTML5 gene list enrichment analysis tool. *BMC bioinformatics* **14:** 128

1038
1039   Cheng TS, Hsiao YL, Lin CC, Hsu CM, Chang MS, Lee CI, Yu RC, Huang CY, Howng SL, Hong YR
1040   (2007) hNinein is required for targeting spindle-associated protein Astrin to the centrosome during the
1041   S and G2 phases. *Exp Cell Res* **313:** 1710-1721

1042
1043   Cheng TS, Hsiao YL, Lin CC, Yu CT, Hsu CM, Chang MS, Lee CI, Huang CY, Howng SL, Hong YR
1044   (2008) Glycogen synthase kinase 3beta interacts with and phosphorylates the spindle-associated protein
1045   astrin. *J Biol Chem* **283:** 2454-2464

1046
1047   Chiu SC, Chen JM, Wei TY, Cheng TS, Wang YH, Ku CF, Lian CH, Liu CC, Kuo YC, Yu CT (2014)
1048   The mitosis-regulating and protein-protein interaction activities of astrin are controlled by aurora-A-
1049   induced phosphorylation. *Am J Physiol Cell Physiol* **307:** C466-478

1050
1051   Chung HJ, Park JE, Lee NS, Kim H, Jang CY (2016) Phosphorylation of Astrin Regulates Its
1052   Kinetochore Function. *J Biol Chem* **291:** 17579-17592

1053
1054   Cuyàs E, Corominas-Faja B, Joven J, Menendez JA (2014) Cell cycle regulation by the nutrient-sensing
1055   mammalian target of rapamycin (mTOR) pathway. *Methods Mol Biol* **1170:** 113-144

1056
1057   Dai LY, Zhao TY, Bisteau X, Sun WD, Prabhu N, Lim YT, Sobota RM, Kaldis P, Nordlund P (2018)
1058   Modulation of Protein-Interaction States through the Cell Cycle. *Cell* **173:** 1481-+

1059
1060   DeBerardinis RJ, Lum JJ, Hatzivassiliou G, Thompson CB (2008) The biology of cancer: Metabolic
1061   reprogramming fuels cell growth and proliferation. *Cell Metab* **7:** 11-20

1062
1063   Dunsch AK, Linnane E, Barr FA, Gruneberg U (2011) The astrin-kinastrin/SKAP complex localizes to
1064   microtubule plus ends and facilitates chromosome alignment. *The Journal of cell biology* **192:** 959-968

1065
1066   Dutchak PA, Estill-Terpack SJ, Plec AA, Zhao X, Yang C, Chen J, Ko B, Deberardinis RJ, Yu Y, Tu
1067   BP (2018) Loss of a Negative Regulator of mTORC1 Induces Aerobic Glycolysis and Altered Fiber
1068   Composition in Skeletal Muscle. *Cell Rep* **23:** 1907-1914

1069
1070   Friese A, Faesen AC, Huis in 't Veld PJ, Fischbock J, Prumbaum D, Petrovic A, Raunser S, Herzog F,
1071   Musacchio A (2016) Molecular requirements for the inter-subunit interaction and kinetochore
1072   recruitment of SKAP and Astrin. *Nat Commun* **7:** 11407

1073
1074   Gao J, Schatton D, Martinelli P, Hansen H, Pla-Martin D, Barth E, Becker C, Altmueller J, Frommolt
1075   P, Sardiello M, Rugarli EI (2014) CLUH regulates mitochondrial biogenesis by binding mRNAs of
1076   nuclear-encoded mitochondrial proteins. *J Cell Biol* **207:** 213-223

1077
1078   Geraghty Z, Barnard C, Uluocak P, Gruneberg U (2021) The association of Plk1 with the astrin–
1079   kinastrin complex promotes formation and maintenance of a metaphase plate. *J Cell Sci* **134**

1080
1081   Gholkar AA, Senese S, Lo Y-C, Vides E, Contreras E, Hodara E, Capri J, Whitelegge JP, Torres JZ
1082   (2016) The X-Linked-Intellectual-Disability-Associated Ubiquitin Ligase Mid2 Interacts with Astrin
1083   and Regulates Astrin Levels to Promote Cell Division. *Cell Rep* **14:** 180-188

1084

Gruber J, Harborth J, Schnabel J, Weber K, Hatzfeld M (2002) The mitotic-spindle-associated protein astrin is essential for progression through mitosis. *J Cell Sci* **115:** 4053-4059

Halim VA, Alvarez-Fernandez M, Xu YJ, Aprelia M, van den Toorn HWP, Heck AJR, Mohammed S, Medema RH (2013) Comparative Phosphoproteomic Analysis of Checkpoint Recovery Identifies New Regulators of the DNA Damage Response. *Sci Signal* **6**

Halim VA, Garcia-Santisteban I, Warmerdam DO, van den Broek W, Heck AJR, Mohammed S, Medema RH (2018) Doxorubicin-induced DNA Damage Causes Extensive Ubiquitination of Ribosomal Proteins Associated with a Decrease in Protein Translation. *Molecular & Cellular Proteomics* **17:** 2297-2308

Harbauer AB, Opalinska M, Gerbeth C, Herman JS, Rao S, Schonfisch B, Guiard B, Schmidt O, Pfanner N, Meisinger C (2014) Cell cycle-dependent regulation of mitochondrial preprotein translocase. *Science* **346:** 1109-1113

Kern DM, Monda JK, Su KC, Wilson-Kubalek EM, Cheeseman IM (2017) Astrin-SKAP complex reconstitution reveals its kinetochore interaction with microtubule-bound Ndc80. *Elife* **6**

Kern DM, Nicholls PK, Page DC, Cheeseman IM (2016) A mitotic SKAP isoform regulates spindle positioning at astral microtubule plus ends. *J Cell Biol* **213:** 315-328

Khan NA, Nikkanen J, Yatsuga S, Jackson C, Wang L, Pradhan S, Kivela R, Pessia A, Velagapudi V, Suomalainen A (2017) mTORC1 Regulates Mitochondrial Integrated Stress Response and Mitochondrial Myopathy Progression. *Cell Metab* **26:** 419-428 e415

Kodani A, Yu TW, Johnson JR, Jayaraman D, Johnson TL, Al-Gazali L, Sztriha L, Partlow JN, Kim H, Krup AL, Dammermann A, Krogan NJ, Walsh CA, Reiter JF (2015) Centriolar satellites assemble centrosomal microcephaly proteins to recruit CDK2 and promote centriole duplication. *Elife* **4**

Koppen M, Metodiev MD, Casari G, Rugarli EI, Langer T (2007) Variable and Tissue-Specific Subunit Composition of Mitochondrial m-AAA Protease Complexes Linked to Hereditary Spastic Paraplegia. *Mol Cell Biol* **27:** 758-767

Kuleshov MV, Jones MR, Rouillard AD, Fernandez NF, Duan Q, Wang Z, Koplev S, Jenkins SL, Jagodnik KM, Lachmann A, McDermott MG, Monteiro CD, Gundersen GW, Ma'ayan A (2016) Enrichr: a comprehensive gene set enrichment analysis web server 2016 update. *Nucleic Acids Res* **44:** W90-97

Leal-Esteban LC, Fajas L (2020) Cell cycle regulators in cancer cell metabolism. *Bba-Mol Basis Dis* **1866**

Lee IH, Finkel T (2013) Metabolic regulation of the cell cycle. *Curr Opin Cell Biol* **25:** 724-729

Li M, Li A, Zhou S, Lv H, Yang W (2019) SPAG5 upregulation contributes to enhanced c-MYC transcriptional activity via interaction with c-MYC binding protein in triple-negative breast cancer. *Journal of hematology & oncology* **12:** 14

1133 MacVicar T, Ohba Y, Nolte H, Mayer FC, Tatsuta T, Sprenger H-G, Lindner B, Zhao Y, Li J, Bruns C,
1134 Krüger M, Habich M, Riemer J, Schwarzer R, Pasparakis M, Henschke S, Brüning JC, Zamboni N,
1135 Langer T (2019) Lipid signalling drives proteolytic rewiring of mitochondria by YME1L. *Nature* **575:**
1136 361-365

1137
1138 Mandal S, Guptan P, Owusu-Ansah E, Banerjee U (2005) Mitochondrial Regulation of Cell Cycle
1139 Progression during Development as Revealed by the tenured Mutation in Drosophila. *Dev Cell* **9:** 843-
1140 854

1141
1142 Manning AL, Bakhoum SF, Maffini S, Correia-Melo C, Maiato H, Compton DA (2010) CLASP1, astrin
1143 and Kif2b form a molecular switch that regulates kinetochore-microtubule dynamics to promote mitotic
1144 progression and fidelity. *The EMBO journal* **29:** 3531-3543

1145
1146 McKinley KL, Cheeseman IM (2017) Large-Scale Analysis of CRISPR/Cas9 Cell-Cycle Knockouts
1147 Reveals the Diversity of p53-Dependent Responses to Cell-Cycle Defects. *Dev Cell* **40:** 405-420

1148
1149 Mitra K, Wunder C, Roysam B, Lin G, Lippincott-Schwartz J (2009) A hyperfused mitochondrial state
1150 achieved at G(1)-S regulates cyclin E buildup and entry into S phase. *Proc Natl Acad Sci U S A* **106:**
1151 11960-11965

1152
1153 Morita M, Gravel SP, Chenard V, Sikstrom K, Zheng L, Alain T, Gandin V, Avizonis D, Arguello M,
1154 Zakaria C, McLaughlan S, Nouet Y, Pause A, Pollak M, Gottlieb E, Larsson O, St-Pierre J, Topisirovic
1155 I, Sonenberg N (2013) mTORC1 Controls Mitochondrial Activity and Biogenesis through 4E-BP-
1156 Dependent Translational Regulation. *Cell Metab* **18:** 698-711

1157
1158 Morita M, Prudent J, Basu K, Goyon V, Katsumura S, Hulea L, Pearl D, Siddiqui N, Strack S, McGuirk
1159 S, St-Pierre J, Larsson O, Topisirovic I, Vali H, McBride HM, Bergeron JJ, Sonenberg N (2017) mTOR
1160 Controls Mitochondrial Dynamics and Cell Survival via MTFP1. *Mol Cell* **67:** 922-935 e925

1161
1162 Morris DR, Geballe AP (2000) Upstream open reading frames as regulators of mRNA translation. *Mol
1163 Cell Biol* **20:** 8635-8642

1164
1165 Nolte H, MacVicar TD, Tellkamp F, Kruger M (2018) Instant Clue: A Software Suite for Interactive
1166 Data Visualization and Analysis. *Sci Rep* **8**

1167
1168 Olsen JV, Vermeulen M, Santamaria A, Kumar C, Miller ML, Jensen LJ, Gnad F, Cox J, Jensen TS,
1169 Nigg EA, Brunak S, Mann M (2010) Quantitative phosphoproteomics reveals widespread full
1170 phosphorylation site occupancy during mitosis. *Sci Signal* **3:** ra3

1171
1172 Pla-Martin D, Schatton D, Wiederstein JL, Marx MC, Khiati S, Kruger M, Rugarli EI (2020) CLUH
1173 granules coordinate translation of mitochondrial proteins with mTORC1 signaling and mitophagy.
1174 *EMBO J* **39:** e102731

1175
1176 Rabanal-Ruiz Y, Byron A, Wirth A, Madsen R, Sedlackova L, Hewitt G, Nelson G, Stingele J, Wills
1177 JC, Zhang T, Zeug A, Fassler R, Vanhaesebroeck B, Maddocks ODK, Ponimaskin E, Carroll B,
1178 Korolchuk VI (2021) mTORC1 activity is supported by spatial association with focal adhesions. *J Cell
1179 Biol* **220**

1180

Rappsilber J, Mann M, Ishihama Y (2007) Protocol for micro-purification, enrichment, pre-fractionation and storage of peptides for proteomics using StageTips. *Nat Protocols* **2:** 1896-1906

Salazar-Roa M, Malumbres M (2017) Fueling the Cell Division Cycle. *Trends Cell Biol* **27:** 69-81

Schatton D, Pla-Martin D, Marx MC, Hansen H, Mourier A, Nemazanyy I, Pessia A, Zentis P, Corona T, Kondylis V, Barth E, Schauss AC, Velagapudi V, Rugarli EI (2017) CLUH regulates mitochondrial metabolism by controlling translation and decay of target mRNAs. *J Cell Biol* **216:** 675-693

Schatton D, Rugarli EI (2018) A concert of RNA-binding proteins coordinates mitochondrial function. *Crit Rev Biochem Mol Biol* **53:** 652-666

Schmidt JC, Kiyomitsu T, Hori T, Backer CB, Fukagawa T, Cheeseman IM (2010) Aurora B kinase controls the targeting of the Astrin-SKAP complex to bioriented kinetochores. *J Cell Biol* **191:** 269-280

Schwaiger M, Rampler E, Hermann G, Miklos W, Berger W, Koellensperger G (2017) Anion-Exchange Chromatography Coupled to High-Resolution Mass Spectrometry: A Powerful Tool for Merging Targeted and Non targeted Metabolomics. *Anal Chem* **89:** 7667-7674

Thedieck K, Holzwarth B, Prentzell MT, Boehlke C, Klasener K, Ruf S, Sonntag AG, Maerz L, Grellscheid SN, Kremmer E, Nitschke R, Kuehn EW, Jonker JW, Groen AK, Reth M, Hall MN, Baumeister R (2013) Inhibition of mTORC1 by astrin and stress granules prevents apoptosis in cancer cells. *Cell* **154:** 859-874

Thein KH, Kleylein-Sohn J, Nigg EA, Gruneberg U (2007) Astrin is required for the maintenance of sister chromatid cohesion and centrosome integrity. *J Cell Biol* **178:** 345-354

Tyanova S, Temu T, Cox J (2016a) The MaxQuant computational platform for mass spectrometry-based shotgun proteomics. *Nat Protocols* **11:** 2301-2319

Tyanova S, Temu T, Sinitcyn P, Carlson A, Hein MY, Geiger T, Mann M, Cox J (2016b) The Perseus computational platform for comprehensive analysis of (prote)omics data. *Nat Meth* **13:** 731-740

Wakim J, Goudenege D, Perrot R, Gueguen N, Desquiret-Dumas V, Chao de la Barca JM, Dalla Rosa I, Manero F, Le Mao M, Chupin S, Chevrollier A, Procaccio V, Bonneau D, Logan DC, Reynier P, Lenaers G, Khiati S (2017) CLUH couples mitochondrial distribution to the energetic and metabolic status. *J Cell Sci* **130:** 1940-1951

Wang ZQ, Fan M, Candas D, Zhang TQ, Qin LL, Eldridge A, Wachsmann-Hogiu S, Ahmed KM, Chromy BA, Nantajit D, Duru N, He FC, Chen M, Finkel T, Weinstein LS, Li JJ (2014) Cyclin B1/Cdk1 Coordinates Mitochondrial Respiration for Cell-Cycle G2/M Progression. *Dev Cell* **29:** 217-232

Wong JMT, Malec PA, Mabrouk OS, Ro J, Dus M, Kennedy RT (2016) Benzoyl chloride derivatization with liquid chromatography-mass spectrometry for targeted metabolomics of neurochemicals in biological samples. *J Chromatogr A* **1446:** 78-90

1227 Xie Z, Bailey A, Kuleshov MV, Clarke DJB, Evangelista JE, Jenkins SL, Lachmann A, Wojciechowicz
1228 ML, Kropiwnicki E, Jagodnik KM, Jeon M, Ma'ayan A (2021) Gene Set Knowledge Discovery with
1229 Enrichr. *Current Protocols* **1:** e90

1230
1231 Yim A, Koti P, Bonnard A, Marchiano F, Dürrbaum M, Garcia-Perez C, Villaveces J, Gamal S, Cardone
1232 G, Perocchi F, Storchova Z, Habermann BH (2020) mitoXplorer, a visual data mining platform to
1233 systematically analyze and visualize mitochondrial expression dynamics and mutations. *Nucleic Acids*
1234 *Res* **48:** 605-632

1235
1236 Ying Z, Yang J, Li W, Wang X, Zhu Z, Jiang W, Li C, Sha O (2020) Astrin: A Key Player in Mitosis
1237 and Cancer. *Front Cell Dev Biol* **8:** 866-866

1238
1239 Young SK, Wek RC (2016) Upstream Open Reading Frames Differentially Regulate Gene-specific
1240 Translation in the Integrated Stress Response. *J Biol Chem* **291:** 16927-16935

1241
1242 Yuan LJ, Li JD, Zhang L, Wang JH, Wan T, Zhou Y, Tu H, Yun JP, Luo RZ, Jia WH, Zheng M (2014)
1243 SPAG5 upregulation predicts poor prognosis in cervical cancer patients and alters sensitivity to taxol
1244 treatment via the mTOR signaling pathway. *Cell Death Dis* **5:** e1247

1245
1246 Zhou H, Wang SC, Ma JM, Yu LQ, Jing JS (2018) Sperm-Associated Antigen 5 Expression Is Increased
1247 in Hepatocellular Carcinoma and Indicates Poor Prognosis. *Medical science monitor : international*
1248 *medical journal of experimental and clinical research* **24:** 6021-6028

1249

1250

1251
1252

SUPPLEMENTARY FIGURES
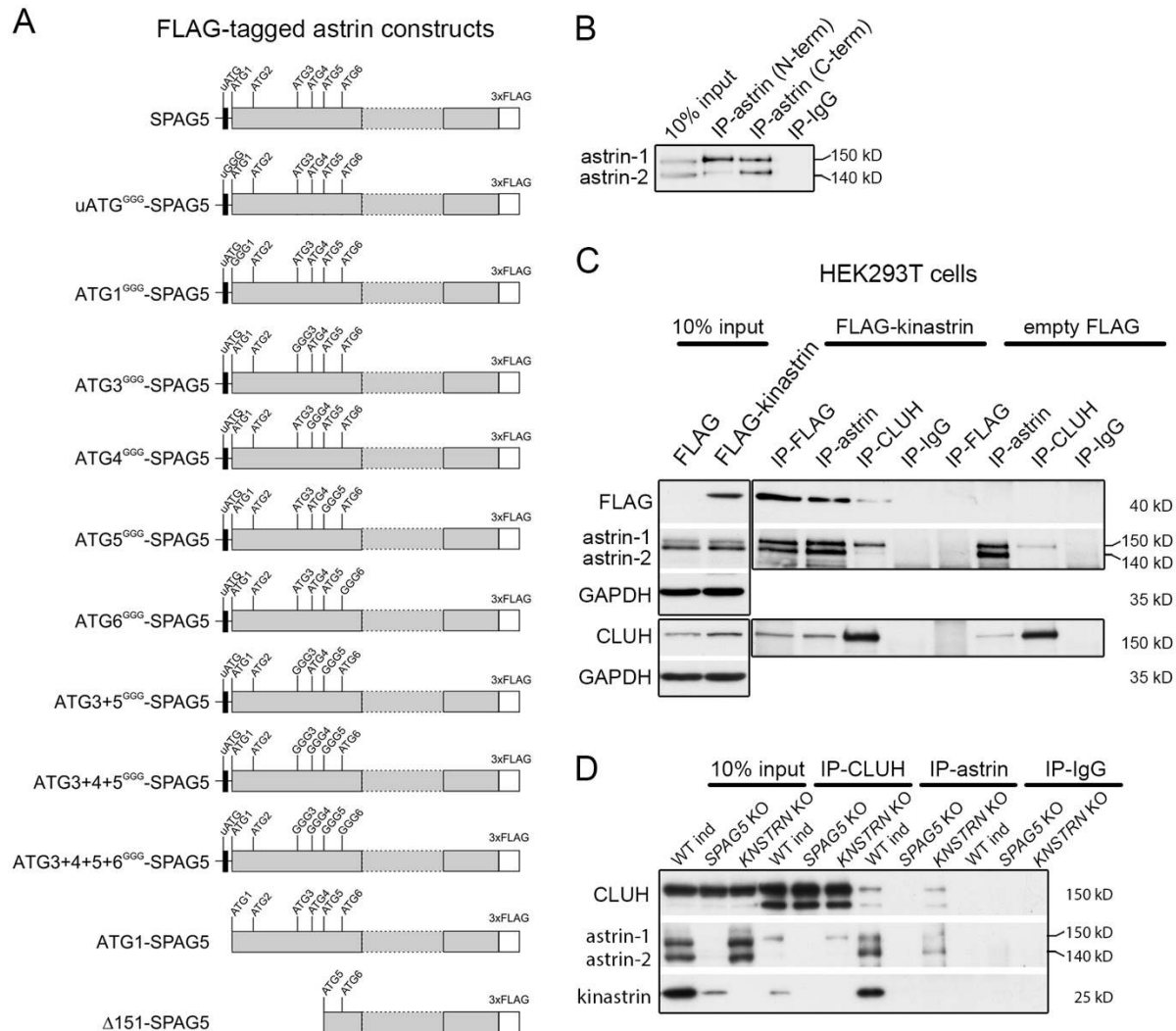
Figure 1-figure supplement 1. CLUH interacts with full length astrin independently of kinastrin.

(**A**) Scheme of C-terminally FLAG-tagged astrin constructs used for overexpression in this study. Positions of ATGs and mutagenized ATGs are indicated. (**B**) Western blot of IP of endogenous astrin using antibodies binding N-terminal or C-terminal epitopes of astrin in HeLa cells. (**C**) Western blots of reciprocal co-IPs in HEK293T cells stably overexpressing FLAG-kinastrin or empty FLAG using antibodies against endogenous CLUH, astrin and overexpressed kinastrin. GAPDH was used as loading control for input samples. (**D**) Western blots of reciprocal co-IPs of endogenous CLUH and astrin in WT, *SPAG5* and *KNSTRN* ind-KO HeLa cells.

1269
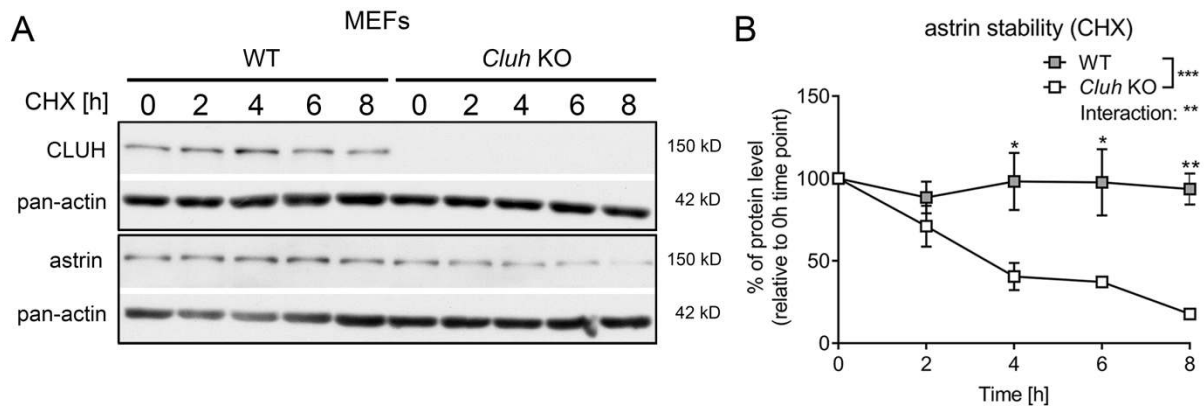
1270

1271 **Figure 2- figure supplement 1. Astrin is unstable in *Cluh* KO MEFs.**

1272 (**A**) Western blots of CHX chase in WT and *Cluh* KO MEFs treated for indicated time points.

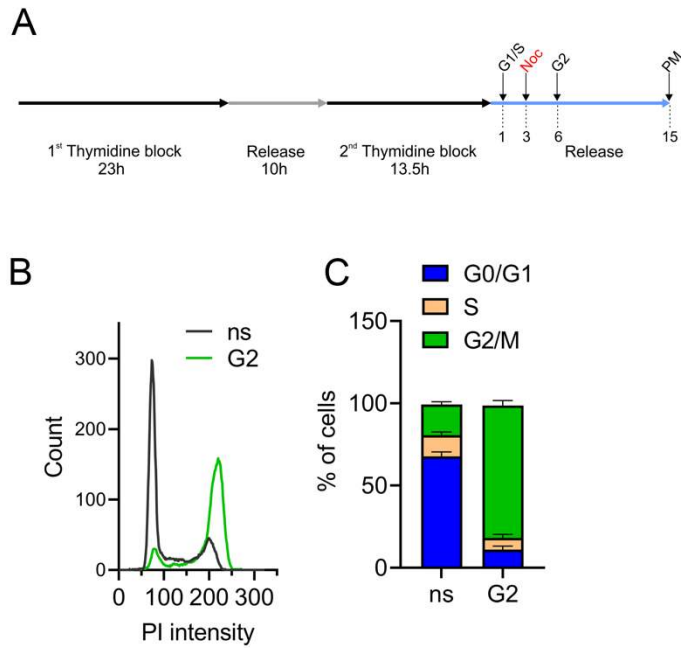1273 Pan-actin staining was used as loading control. (**B**) Quantification of CHX chase western blots

1274 as shown in A (n=3 independent experiments). Two-way ANOVA with post hoc Tukey`s

1275 multiple comparison test was performed with $P \leq 0.05$: *; $P \leq 0.01$: **; $P \leq 0.001$: ***. Genotype

1276 x time interaction significance is also shown. Graphs show mean ± SEM.

1277

1278

1279

1280 **Figure 3- figure supplement 1. Controls of effective synchronization of IP samples.**

1281 (**A**) Synchronization protocol used for IP experiments. Cells enriched in G1/S and G2 were

1282 collected after 1 h and 6 h after release of the 2nd thymidine block, respectively. Cells enriched

1283 in prometaphase (PM) were treated with nocodazole (noc) after 3 h of release and collected

1284 after additional 12 h. (**B, C**) PI intensity profiles (B) and cell cycle distribution analysis (C) of

1285 non-synchronized (ns) or G2-enriched WT cells used for IP followed by mass spectrometry

1286 (n=4 independent replicates).
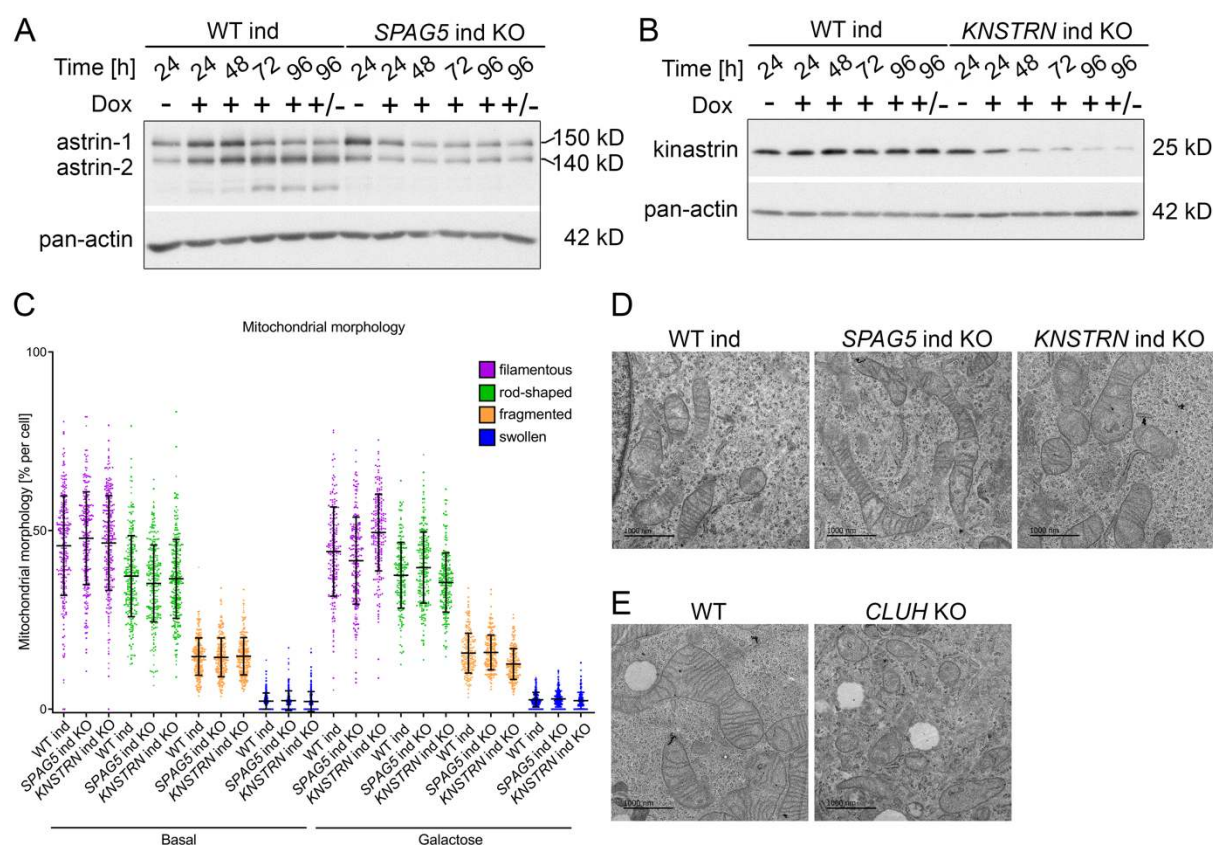
1287
1288

Figure 5-figure supplement 1. *SPAG5* **and** *KNSTRN* **ind KO HeLa cells show normal mitochondrial morphology.**

(**A, B**) Western blots of induction time course in WT and *SPAG5* (A) or *KNSTRN* (B) ind-KO HeLa cells. Cells were treated with doxycycline for indicated time points. +/- means that cells were treated with doxycycline for 72 h and not treated for the remaining 24 h. Pan-actin was used as loading control. (**C**) Quantification of mitochondrial morphology of experiments shown in Figure 5A (n=3 independent experiments; in total the following number of cells have been analyzed: basal: WT ind: 248, *SPAG5* ind KO: 244, *KNSTRN* ind KO: 274; galactose: WT ind: 186, *SPAG5* ind KO: 214, *KNSTRN* ind KO: 202). Scatter dots represent cells of all three replicates and symbols differ for cells belonging to different replicates. Graph shows mean ± SD. (**D, E**) Representative electron micrographs of WT, *SPAG5* and *KNSTRN* ind-KO (D) or WT and *CLUH* KO (E) HeLa cells. Scale bar, 1000 nm.

1301

55
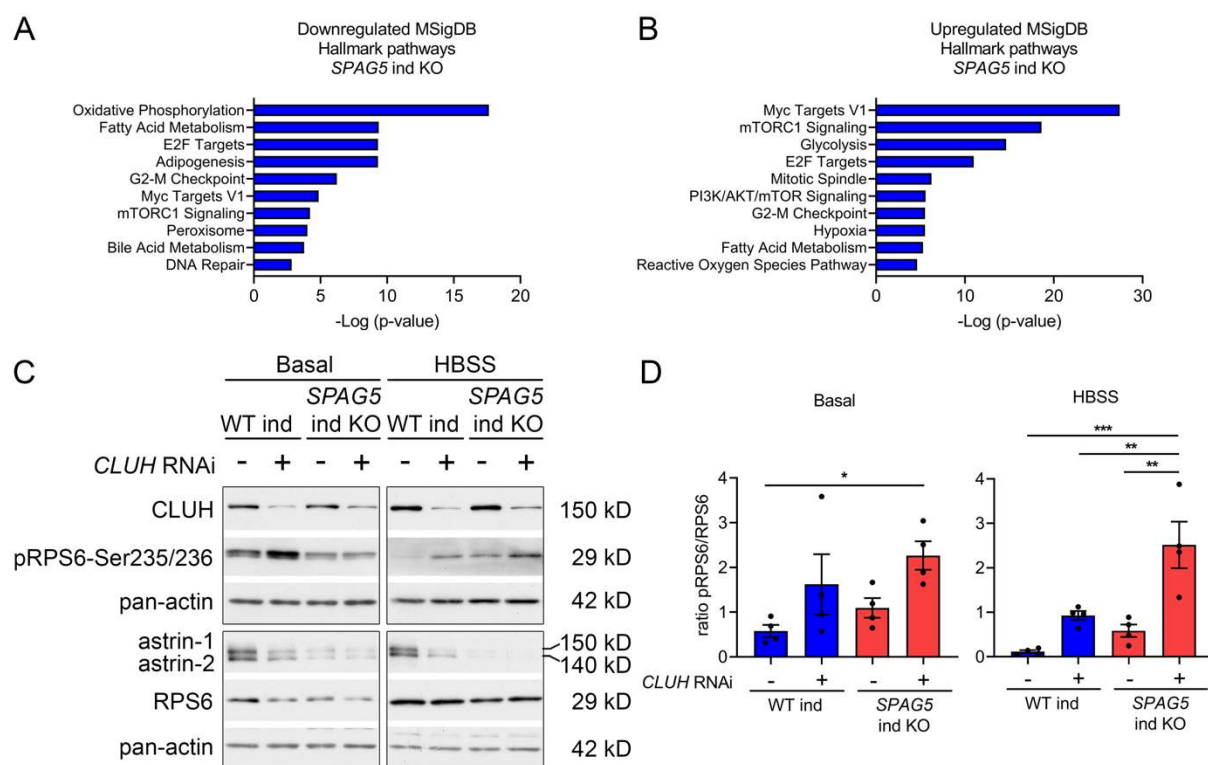
1302

1303

1304 **Figure 6-figure supplement 1. Loss of SPAG5 and CLUH lead to hyperactivation of**

1305 **mTORC1 signaling.**

1306 (**A, B**) MSigDB Hallmark pathways of downregulated (E) or upregulated (F) proteins (with a

1307 cut-off of p≤0.05; q≤0.15) detected in proteomics analysis of *SPAG5* ind-KO cells (Fig 4A and

1308 Supplementary Table3) using the EnrichR webtool. (**C**) Western blots of WT and *SPAG5* ind-

1309 KO HeLa cells transfected with siRNA against CLUH or untargeted control siRNA. Cells were

1310 induced for four days with doxycycline, additionally downregulated for the last three days and

1311 grown for the last 8 h in basal or HBSS media without doxycycline. Pan-actin was used as

1312 loading control. (**D**) Quantification of experiments as shown in C (n=4 independent

1313 experiments). Antibody signal was normalized to pan-actin signal, and signal of phospho-

1314 protein was normalized to signal of the total protein. Bars show mean ± SEM and dots represent

1315 values of individual replicates. One-way ANOVA with post hoc Tukey`s multiple comparison

1316 tests were performed with P≤0.05: *; P≤0.01: **; P≤0.001: ***.

1317
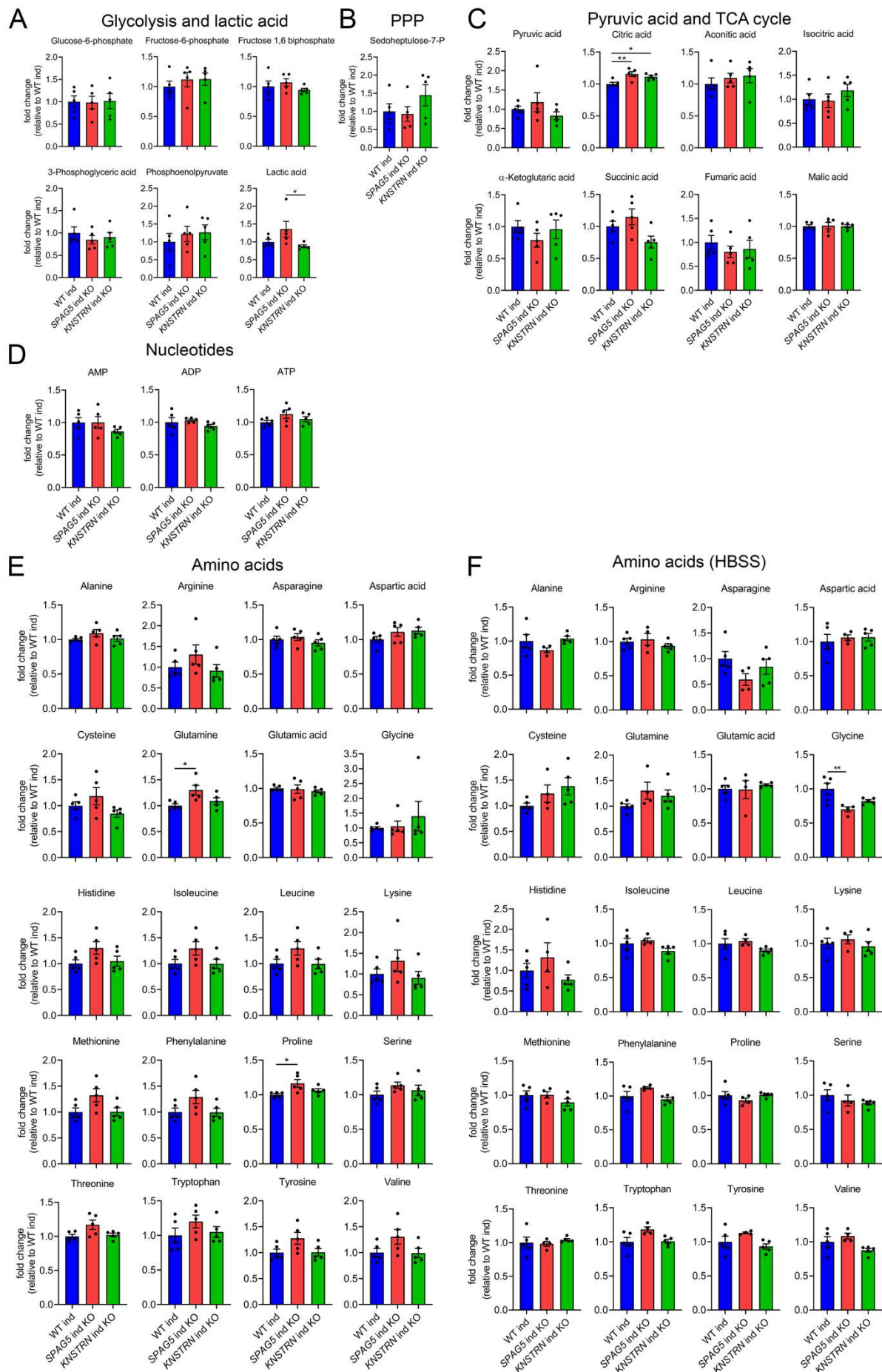
1318 **Figure 6-figure supplement 2. Astrin and kinastrin depletion does not affect cellular**

1319 **metabolism under basal conditions.**

1320 (**A-F**) Targeted metabolomics of WT, *SPAG5* and *KNSTRN* ind-KO HeLa cells under basal

1321 conditions (A-E) or after 8h HBSS starvation (F) showing glycolytic intermediates and lactic

1322 acid (A), sedoheptulose-7-P (B), pyruvic acid and TCA cycle intermediates (C), nucleotide (D)

1323 and amino acid levels (E-F). Bars show mean ± SEM and dots represent values of individual

1324 replicates. One-way ANOVA with post hoc Tukey`s multiple comparison tests were performed

1325 on log converted fold changes with P≤0.05: *; P≤0.01: **.

1326

1327
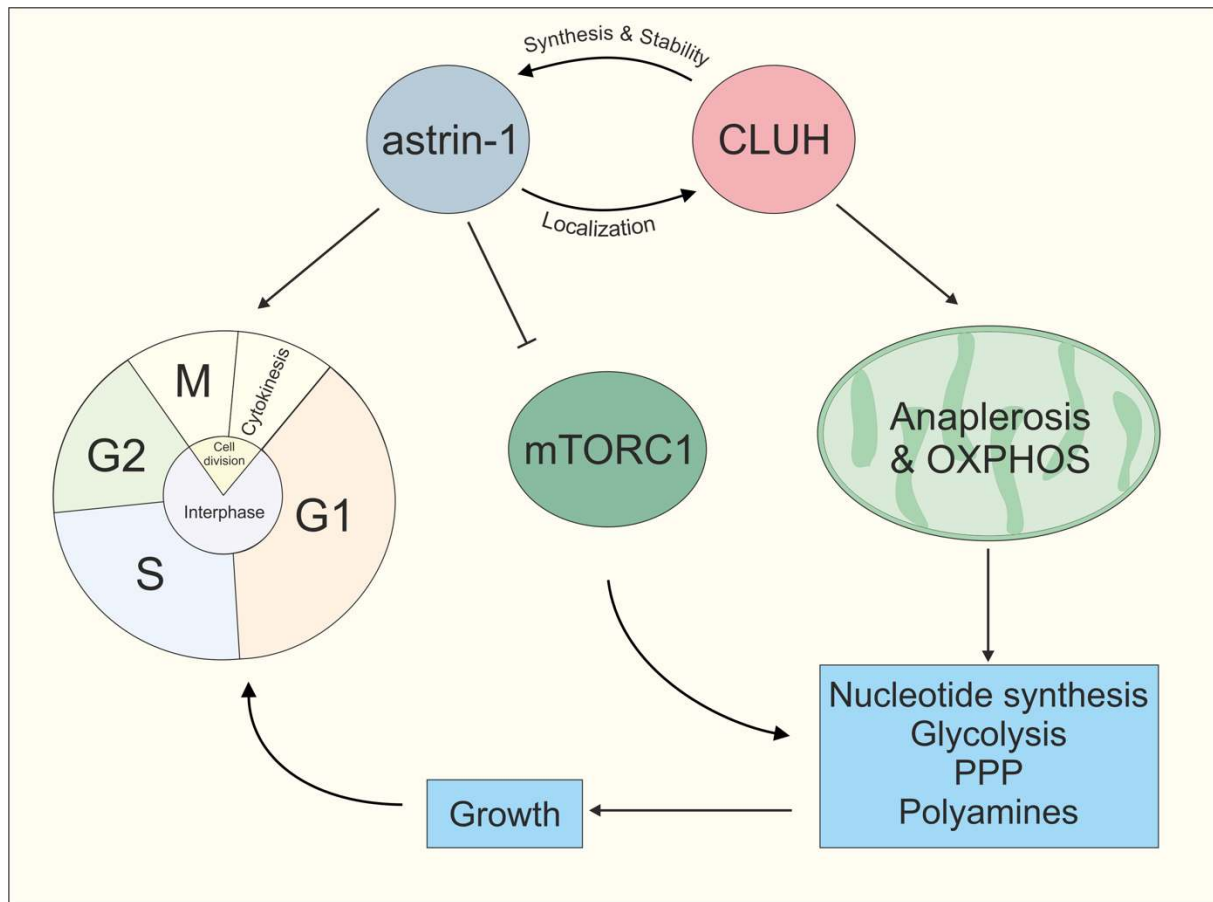
1328
1329

Figure 8- figure supplement 1. Model of CLUH/astrin-1 complex function in proliferating cells.

CLUH and astrin-1 form a complex and regulate each other reciprocally. On the one hand, CLUH is required for astrin synthesis and for protein stability. Additionally, CLUH promotes mitochondrial anaplerotic reactions and OXPHOS function by ensuring CLUH-target expression. This provides energy and building blocks to increase anabolic pathways like nucleotide synthesis, glycolysis, pentose phosphate pathway and polyamine synthesis required for growth in G1 and allowing cell cycle progression at the G1/S boundary. Astrin-1 on the other hand regulates CLUH localization, controls metaphase to anaphase progression in M phase and inhibits mTORC1.

1340

1341
1342
1343
1344
1345
1346

SUPPLEMENTARY TABLES

Supplementary Table 1: Interactors of endogenous human CLUH in HeLa cells after SILAC labeling

Supplementary Table 2: Interactors of endogenous human CLUH in G2-enriched HeLa cells

Supplementary Table 3: Proteomics data of *SPAG5* and *KNSTRN* ind-KO HeLa cells

Supplementary Table 4: IC-TQ_Transitions compound list

SOURCE DATA

Figure 1-source data 1. Uncropped blots for Figure 1A

Figure 1-source data 2. Uncropped blots for Figure 1B

Figure 1-source data 3. Uncropped blots for Figure 1D

Figure 1-source data 4. Uncropped blots for Figure 1E

Figure 1-source data 5. Uncropped blots for Figure 1F

Figure 1-source data 6. Uncropped blots for Figure 1G

Figure 1-figure supplement 1-source data 1. Uncropped blots for Figure 1-figure supplement 1B

Figure 1-figure supplement 1-source data 2. Uncropped blots for Figure 1-figure supplement 1C

Figure 1-figure supplement 1-source data 3. Uncropped blots for Figure 1-figure supplement 1D

Figure 2-source data 1. Uncropped blots for Figure 2A

Figure 2-source data 2. Uncropped blots for Figure 2H

Figure 2-figure supplement 1-source data 1. Uncropped blots for Figure 2-figure supplement 1A

1395   **Figure 3-source data 1.** Uncropped blots for Figure 3A

1396

1397   **Figure 4-source data 1.** Uncropped blots for Figure 4D

1398

1399   **Figure 5-source data 1.** Uncropped blots for Figure 5D

1400

1401   **Figure 5-figure supplement 1-source data 1.** Uncropped blots for Figure 5-figure
1402   supplement 1A

1403

1404   **Figure 5-figure supplement 1-source data 2.** Uncropped blots for Figure 5-figure
1405   supplement 1B

1406

1407   **Figure 6-figure supplement 1-source data 1.** Uncropped blots for Figure 6-figure
1408   supplement 1C

1409

1410   **Figure 8-source data 1.** Uncropped blots for Figure 8F

1411

1412

1413

1414

1415

1416

1417

1418